J. Fluid Mech. (1998), *vol.* 354, *pp.* 175–208. Printed in the United Kingdom

Turbulent mixing in a shear-free stably stratified two-layer fluid

By DAVID A. BRIGGS,† JOEL H. FERZIGER,‡ JEFFREY R. KOSEFF AND STEPHEN G. MONISMITH

Environmental Fluid Mechanics Laboratory, Department of Civil and Environmental Engineering, Stanford University, Stanford, CA 94305-4020, USA

(Received 30 August 1996 and in revised form 22 August 1997)

Direct numerical simulation is used to examine turbulent mixing in a shear-free stably stratified fluid. Energy is continuously supplied to a small region to maintain a well-developed kinetic energy profile, as in an oscillating grid flow (Briggs *et al.* 1996; Hopfinger & Toly 1976; Nokes 1988). A microscale Reynolds number of 60 is maintained in the source region. The turbulence forms a well-mixed layer which diffuses from the source into the quiescent fluid below. Turbulence transport at the interface causes the mixed layer to grow under weakly stratified conditions. When the stratification is strong, large-scale turbulent transport is inactive and pressure transport becomes the principal mechanism for the growth of the turbulence layer. Down-gradient buoyancy flux is present in the large scales; however, far from the source, weak counter-gradient fluxes appear in the medium to small scales. The production of internal waves and counter-gradient fluxes rapidly reduces the mixing when the turbulent Froude number is lower than unity. When the stratification is weak, the turbulence is strong enough to break up the density interface and transport fluid parcels of different density over large vertical distances. As the stratification intensifies, turbulent eddies flatten against the interface creating anisotropy and internal waves. The dominant entrainment mechanism is then scouring. Mixing efficiency, defined as the ratio of buoyancy flux to available kinetic energy, exhibits a similar dependence on Froude number to other stratified flows (Holt *et al.* 1992; Lienhard & Van Atta 1990). However, using the anisotropy of the turbulence to define an alternative mixing efficiency and Froude number improves the correlation and allows local scaling.

1. Introduction

Turbulent mixing across a density interface is a common occurrence in geophysical flows and affects the dispersion of contaminants and nutrients. While large advective motions tend to dominate horizontal mixing, entrainment by turbulence is a major contributor to the vertical exchange between layers in stratified fluids. Stable density stratification, a distinguishing characteristic of geophysical flows, impedes turbulent motions but a portion of the kinetic energy of the turbulence is converted into potential energy through stirring and mixing.

† Present address: Contra Costa Water District, PO Box H2O, Concord, CA, USA.
‡ Also: Department of Mechanical Engineering, Stanford University, Stanford, CA 94305-3030, USA.

Turbulent kinetic energy that can be used for mixing can be produced in many ways. For example, wind-induced shear stress on water surfaces produces a homogeneous well-mixed layer which diffuses downward into quiescent regions. Turbulence is also created by intense surface and internal wave breaking and by tidal forcing in estuaries. Localized turbulence generation in the laboratory can be accomplished with an oscillating grid (see for example, Hopfinger & Toly 1976; Thompson & Turner 1975). The turbulent kinetic energy diffuses from the grid and propagates into quiescent portions of the fluid; in these experiments a sharp density interface was maintained between the well-mixed turbulent layer and the quiescent region (other work has linear stratification, see E & Hopfinger 1986; Linden 1975). Shear-free experiments allow entrainment by the turbulence at the interface to be isolated from other phenomena. Also, as shown in our earlier paper (Briggs *et al.* 1996) they allow careful testing of models for turbulent diffusion.

There are disadvantages to using oscillating grids to create turbulence. The length scale imposed by the grid may dominate the turbulence structure and persist far from the source (Turner 1968). The grid stroke, mesh, and frequency, as well as distance from the grid, also affect the turbulence (Nokes 1988). Additionally, the velocity decay rates and the far-field anisotropy depend on the grid stroke and distance from the grid (De Silva & Fernando 1992). Although shear-driven entrainment flows are a good representation of naturally occurring well-mixed layers, the presence of shear complicates the analysis of turbulence. Instabilities caused by the mean shear (Kelvin–Helmholtz billowing) are largely responsible for the growth of the mixed layer (Kantha *et al.* 1977; Sullivan & List 1994).

Local values of the Reynolds, Richardson, and Prandtl numbers determine the turbulence structure and mixing mechanisms (Breidenthal 1992). At low Richardson number, large overturning motions are possible because the turbulence is not affected by buoyancy. Parcels of fluid can be transported over large vertical distances and engulfment may occur at weakly stratified interfaces. Buoyancy forces prevent the large scales from overturning when the potential energy change that would result from an overturning event exceeds the kinetic energy of the eddy. Weak eddies tend to flatten at the interface instead of overturning. Flattening of eddies at the interface was quantified by Hannoun, Fernando & List (1988) through the use of vertical and horizontal energy spectra. Low wavenumbers in the vertical energy spectra are attenuated while the same scales in the horizontal spectra are amplified near the interface. Other mechanisms may operate when stratification influences the turbulence. Linden (1973) proposed a recoiling mechanism in which a large-scale eddy deforms the interface and then rebounds into the mixed layer. Interfacial wave breaking can also entrain fluid locally (Fernando 1991). Under strong stratification, scouring may occur near a sharp interface when an eddy pulls off small pieces of fluid of higher or lower density. H. J. S. Fernando (1996, personal communication) recently proposed a model in which the turbulence generates internal waves at the interface. The waves grow until they break, causing local mixing. Fernando (1991) and Breidenthal (1992) give comprehensive reviews of mixing mechanisms in stratified fluids.

In stratified turbulent flows, parcels of fluid are transported by large-scale motions into regions of different density. If molecular diffusion is slow relative to that of momentum (large Prandtl or Schmidt number) and if the turbulence kinetic energy is insufficient to sustain stirring, then restratification or counter-gradient fluxes will appear. Some experiments with homogeneous unsheared stratified turbulence show that the largest scales restratify while the smaller scales continue to actively mix (Lienhard & Van Atta 1990). Other unsheared stably stratified experiments did not

exhibit restratification at any scale (Itsweire & Helland 1989). Finally, simulations of homogeneous shear flow produce weak counter-gradient fluxes in the smallest scales (Holt, Koseff & Ferziger 1992). Counter-gradient fluxes are increasingly present as Prandtl number increases (Gerz, Schumann & Elghobashi 1989) but can appear for Pr as low as 1 (Holt *et al.* 1992).

The turbulent Froude number has been established as a useful parameter for the analysis of stratified turbulence and mixing (Ivey & Imberger 1991). The mixing efficiency (flux Richardson number), which represents the buoyancy flux produced by the local turbulent kinetic energy, depends on the Froude number. The maximum conversion rate of kinetic energy into buoyancy flux in both experimental and numerical homogeneous flows is approximately 25% and occurs at $Fr \approx 1$ (Ivey *et al.* 1992). When restratification becomes active, the mixing efficiency decreases sharply. Furthermore, there is support for Prandtl number dependence of the peak mixing efficiency (higher Pr corresponds to higher mixing efficiency) because density fluctuations and $R_{v\rho} = \overline{v\rho}/v'\rho'$ are rapidly reduced for $Pr < 1$ (Lienhard & Van Atta 1990).

There are three purposes of this study. The first is to quantify the transport processes, buoyancy flux, energy dissipation, and mixing near a density interface. Using direct numerical simulation (DNS), the turbulence structure and mixing mechanisms can also be studied in detail. The second purpose is to demonstrate that turbulence quantities collapse with local scaling. Data from the present shear-free study and from sheared flows will be shown to have the same turbulent Froude number dependence. The last purpose is to quantify the internal wave field. In shear-free turbulence flows with linear stratification, breaking internal waves have been shown to contribute to the mixing (De Silva & Fernando 1992).

The paper is separated into the following sections. The parameters and definitions are introduced in §2. The next section reviews the numerical method for turbulence generation and discusses the kinetic energy budgets. Section 4 develops the entrainment rate dependence on the Richardson number and describes the scale of buoyancy flux and turbulence transport. The relationship between stratification and counter-gradient fluxes (small-scale reversals) is also considered. In §5, the dependence on the turbulent Froude number of mixing efficiency, length scales, and turbulence structure is analysed. Finally, §6 examines the internal waves that are generated by the turbulence.

2. Relevant equations and definitions

The simulations presented in this paper are based on the Navier–Stokes equations with the Boussinesq approximation. The code used is a modified version of one written by Rogallo (1981) for homogeneous flows. The modifications include the addition of a scalar field and a scheme that enables the code to simulate a mean scalar gradient, including a thermocline. Periodic boundary conditions are imposed in all directions. The details of the equations, numerical method, and the forcing used to simulate the oscillating grid are given in our earlier paper (Briggs *et al.* 1996) and are not repeated here in the interests of brevity. Although the earlier paper included both temporal and spatial simulations, in this paper only spatial simulations which are intended to mimic oscillating grid experiments are performed. Thus the flow is steady in the statistical sense.

For shear-free turbulence with one inhomogeneous direction, the mean turbulent

kinetic energy equation reduces to

$$\frac{\partial}{\partial t}\left(q^2/2\right) = -\frac{1}{2}\frac{\partial}{\partial y}\overline{(u^2+v^2+w^2)v} - \frac{1}{\rho_o}\frac{\partial \overline{pv}}{\partial y} - \frac{g}{\rho_o}\overline{v\rho} - \nu\overline{\frac{\partial u_i}{\partial x_k}\frac{\partial u_i}{\partial x_k}} + \nu\frac{\partial^2(q^2/2)}{\partial y^2} + S_k(y) \qquad (2.1)$$

where $q^2 = \overline{u_i u_i}$, $S_k(y)$ denotes the contribution to the budget from the source, ρ represents fluctuating density, and ρ_o and ρ_s are the reference density of the quiescent fluid and the density in the source region, respectively. The normalized density is $\theta = (\rho - \rho_s)/(\rho_o - \rho_s)$. The vertical direction is aligned with the y-axis. A quantity with an overbar denotes the ensemble average of that quantity over the homogeneous horizontal plane. Primes denote r.m.s. values.

The Taylor microscales are defined as

$$\lambda_{ij,1} \equiv \frac{u_i'}{\left(\overline{(\partial u_j/\partial x_1)^2}\right)^{1/2}} \qquad (2.2)$$

and are used to form a Reynolds number, $Re_\lambda = q\lambda_{11,1}/\nu$.

The strength of the stratification relative to the turbulence can be quantified in many ways. The first, and most general, is with the bulk Richardson number,

$$Ri_b = \frac{\Delta\overline{\rho}}{\rho_o}\frac{g\lambda_s}{q_s^2}. \qquad (2.3)$$

In this definition, $\Delta\overline{\rho}$ represents the initial density difference across the interface and the s subscript refers to quantities evaluated in the centre of the source region. In equation (2.3), the Taylor microscale is taken as $\lambda_s = \lambda_{11,1}$, that is a horizontal length scale. The buoyancy time scale is the inverse of the Brünt–Väisälä frequency, N, which is defined as

$$N = \left(\frac{-g}{\rho_o}\frac{\partial\overline{\rho}}{\partial y}\right)^{1/2}. \qquad (2.4)$$

In this work, the gravitational acceleration, g, is changed to vary the bulk Richardson number Ri_b; the turbulence source strength and initial density difference across the interface are held fixed. Simulations were performed with six different Ri_b: 0, 0.06, 0.24, 0.47, 0.95, and 1.18. In the $Ri_b = 0$ case the density field behaves as a passive scalar.

The bulk Richardson number is used to distinguish simulations but is not useful for analysis purposes. A more appropriate parameter for the investigation of turbulence mixing is the isotropic Froude number which measures the strength of local turbulence relative to stratification. This parameter is defined as the ratio of the local buoyancy time scale (N^{-1}) to the local turbulence time scale (ℓ/q):

$$Fr_t = \frac{q}{N\ell} \qquad (2.5)$$

and is a function of distance from the simulated grid.

The overturning scale of the turbulence, ℓ, is approximated by the Ellison scale, which is defined as

$$\ell \approx L_E = -\frac{\rho'}{\partial\overline{\rho}/\partial y} \qquad (2.6)$$

and is also used to characterize stratified turbulence. The vertical turbulent Froude

number,

$$Fr_v = \frac{v'}{N\ell}, \tag{2.7}$$

which emphasizes the contribution of the vertical component of the turbulence, will prove to be a very useful parameter. Like Fr_t, it varies in the vertical direction. The same values of Fr_v occur in simulations with different Ri_b, enabling the study of its effectiveness as a correlating parameter. Lastly, a local Richardson number (Hopfinger & Toly 1976), can be defined as

$$Ri_l = \frac{\Delta\overline{\rho}}{\rho_o}\frac{g}{u^2}\ell \tag{2.8}$$

where ℓ, the overturning scale, and u are averaged over the interface thickness, h. The interface thickness is taken to be

$$h = \Delta\overline{\rho}/(\partial\overline{\rho}/\partial y)_{max}, \tag{2.9}$$

a definition introduced by E & Hopfinger (1986).

3. Simulation of oscillating grid experiments

In laboratory experiments, oscillating grids are used to generate turbulence in a tank of quiescent fluid (Hopfinger & Toly 1976; Hannoun *et al.* 1988). The numerical method used in this work and the earlier work (Briggs *et al.* 1996) adds energy continuously and locally into the flow by boosting the Fourier coefficients according to

$$\hat{u}_i(\kappa, y) = \hat{u}_i(\kappa, y)\{1 + g(y)j(\kappa)\} \tag{3.1}$$

where $g(y)$ is a Gaussian function which restricts the energy addition to a slim vertical layer. For all cases considered here, the thickness δ of the Gaussian was $\delta/\lambda_s = 6$. The function $j(\kappa)$ is used to restrict energy addition to the mid-range of scales and is defined as

$$j(\kappa) = \begin{cases} 1, & \kappa_l \leqslant \kappa \leqslant \kappa_h \\ 0, & \text{otherwise;} \end{cases} \tag{3.2}$$

where $\kappa = (\kappa_x^2 + \kappa_z^2)^{1/2}$ is the horizontal wavenumber and $\kappa_l = 3$ and $\kappa_h = 42$. The simulations presented here were computed on a 128^3 grid with a cut-off wavenumber of 61. To maintain periodicity in the inhomogeneous direction, two mixed layers are created in the domain (one above and one below the source). Quantities from these two mixed layers can be averaged and in this paper we shall refer to the average as if it were a single mixed layer.

On average, an equal amount of energy is added to each velocity component. However, individual boosting events, which occur every fifth time step, introduce a small degree of randomness into the turbulence by varying the magnitude of $g(y)$ among the velocity components. The details of how this is done are explained in Briggs *et al.* (1996) so we shall not present them again. After about five eddy turnover time scales, a well-developed kinetic energy profile develops, see figure 1. Distance from the source is measured by the coordinate $y^* = (y - y_s)/l_s$, where y_s is the location of the maximum source intensity and l_s, the source half-width, is the width of the region that contains 50% of the source energy. The density field, also shown in figure 1, initially has a sharp interface that simulates a thermocline. The interface is far

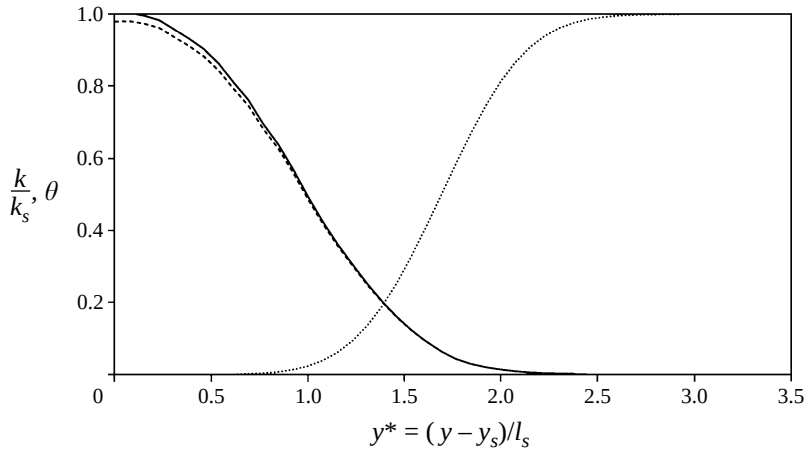

FIGURE 1. Normalized kinetic energy before (– – – –) and after (——) a boosting event. k_s is the maximum source intensity and is evaluated after boosting. The normalized density profile is also sketched for reference (· · · ·).

Re_{λ_s}	60
Pr	1.0
$\tau = k_s/\epsilon_s$ (s)	0.21
$\Delta\overline{\rho}/\rho_o$	0.062

TABLE 1. Time-averaged quantities in the source region above the mixing layer

enough from the source to ensure that the local turbulent kinetic energy is derived almost entirely from transport.

The steadiness of the flow needs to be addressed. When the flow becomes well-developed, the source energy is no longer completely dissipated because transport processes have developed and the kinetic energy and scalar interfaces have begun to propagate into the the quiescent region. We consider the flow to be quasi-steady at this point – 'quasi' because the interface is always moving and 'steady' because relative to the turbulence velocity scale the interface motion is much slower. In this case the initial conditions are no longer important and data on the early development of the flows are not given. More details on the initial conditions of the turbulence can be found in Briggs *et al.* (1996).

The parameters in the developed homogeneous source region are displayed in table 1. As the bulk Richardson number is varied, the filter functions that define the turbulence source, $g(y)$ and $j(\kappa)$, are held fixed. Therefore, the turbulence length scales and energy in the source region are nearly identical in all simulations and are independent of stratification intensity. Time normalized by the initial eddy turnover time, $\tau = k_o/\epsilon_o$, is denoted as $t^* = t/\tau$.

Since the interface location moves and its structure changes as the flow evolves, it is not possible to use long term-time averaging to reduce the uncertainty in the statistical results. (A limited amount of averaging over a time scale roughly equal to the eddy turnover time scale was used.) As was shown in Briggs *et al.* (1996), the uncertainty in the results can be reduced by making several simulations and computing an ensemble average. Unfortunately, computer time limitations prevented

us from performing multiple simulations of the present flows. The uncertainty depends on which quantity one considers. Some results (such as the spectra) are quite smooth; others (including the higher-order moments that appear in some of the budgets) are less smooth.

One way to estimate the uncertainty is to argue that it is due to having a limited number of large structures in the flow. From the contour plots presented in §5.4, it is possible to estimate the number of large eddies in the interface region; it is typically 10 to 20, indicating that the statistical errors may be as large as 20–30%. An alternative approach is to look at the budgets and spectra and estimate the uncertainty from their lack of smoothness. This method indicates that the uncertainties are probably in the range of 10–20%.

3.1. *Kinetic energy budgets*

The relationship between turbulence and stratification can be investigated by examining the terms in the kinetic energy budget, equation (2.1). In figure 2(*a*), the terms in the kinetic energy budget for $Ri_b = 0$ are shown. All curves are normalized by the source term (S_k) at $y^* = 0$. Most of the energy added in the source region ($y^* < 1$) goes directly into dissipation because this region is nearly homogeneous and transport is negligible. In the mixing layer ($1.5 < y^* < 2.5$), the source goes rapidly to zero and turbulence transport is important. Turbulent transport is the only source of turbulence energy in the mixing layer and its gradient balances the dissipation. Pressure transport acts in opposition to the turbulent transport because low-pressure wakes are created behind eddies that penetrate the interface. This mechanism is similar to ones found in temporal simulations (Briggs *et al.* 1996). The contribution of diffusive transport is negligible.

Figure 2(*b*) shows the kinetic energy budget under weakly stratified conditions ($Ri_b = 0.24$). When stable stratification is introduced, a fraction of the kinetic energy is converted into potential energy by means of down-gradient buoyancy flux. In the mixing layer, the source is small and transport is balanced by the buoyancy flux and dissipation. The buoyancy flux is as much as 20% of the dissipation in the mixing layer. In comparison, the buoyancy flux in homogeneous shear flows is about 10% of the dissipation and is Richardson-number dependent (Holt *et al.* 1992). Relative to the unstratified flow the pressure transport is reduced and the turbulence transport decays more rapidly near the interface, indicating that the interface acts as a barrier to turbulence transport. In the highly stratified case ($Ri_b = 1.18$), shown in figure 2(*c*), the buoyancy flux and dissipation are of similar size in the mixing layer. Transport is again sharply reduced at the interface. However, pressure transport changes sign as distance from the source increases. This is possibly due to the flattening of eddies at the interface which causes pressure pulses that transport energy into the interface (Briggs *et al.* 1996). At the fringe of the kinetic energy front, pressure transport is the only significant transport mechanism.

4. Entrainment and mixing

4.1. *Richardson number effects*

Parameterization of the entrainment rate is required for prediction of turbulence and scalar transport. The relevant correlating parameters include the Richardson, Prandtl, and Reynolds numbers. In this study, Pr and Re are fixed and only Ri_b is varied.

The entrainment velocity is the propagation speed of turbulence into a quiescent region (Ellison & Turner 1959). To determine the mixed layer depth D, the mean

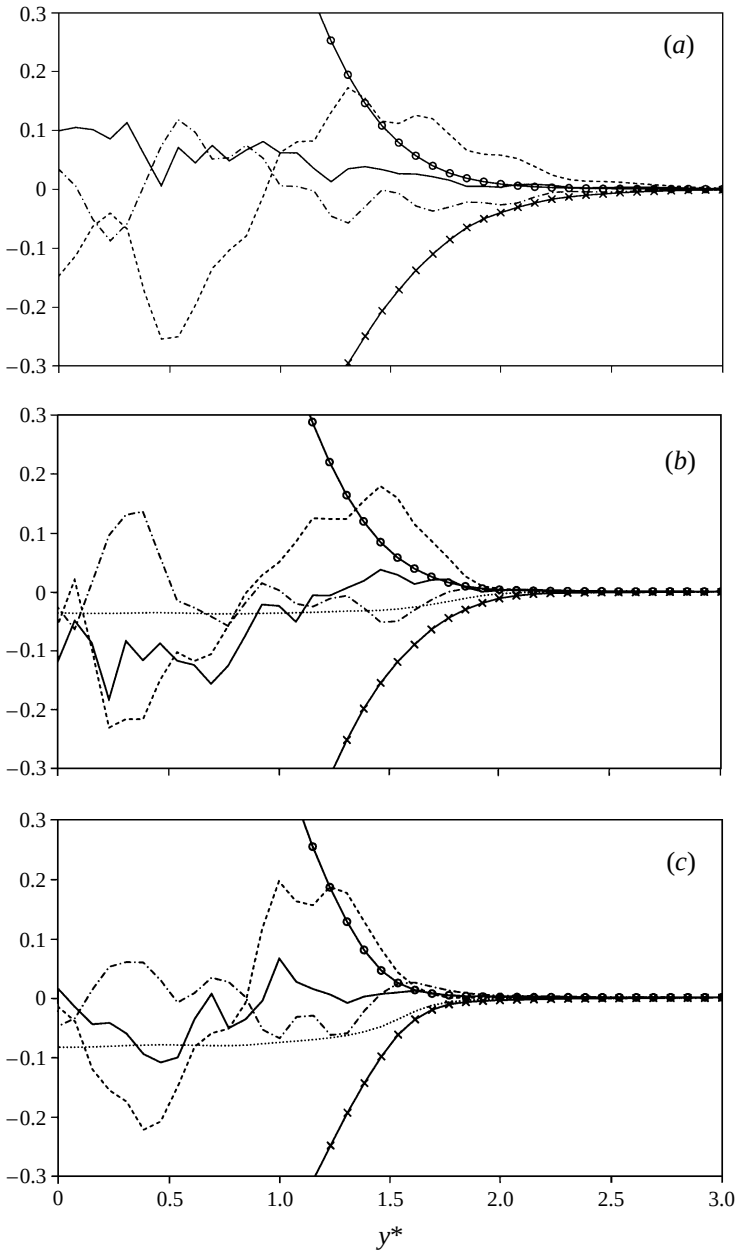

FIGURE 2. Terms in the kinetic energy budget for (*a*) $Ri_b = 0.0$; (*b*) $Ri_b = 0.24$; (*c*) $Ri_b = 1.18$; at $t^* = 14.7$. Curves represent: ——, $\partial(q^2/2)/\partial t$; – – – – –, turbulence transport; — · —, pressure transport; — × —, dissipation; — ○ —, source; and, in (*b*) and (*c*), · · · ·, buoyancy flux.

scalar profile at a given time is compared to the initial profile. The locations in the evolved profile that have lower concentration are considered to be in the interface region. The mixed layer depth, D, is defined as the average of these depths. The definition of the entrainment velocity in this study is

$$\frac{\mathrm{d}D}{\mathrm{d}t} = v_e. \tag{4.1}$$

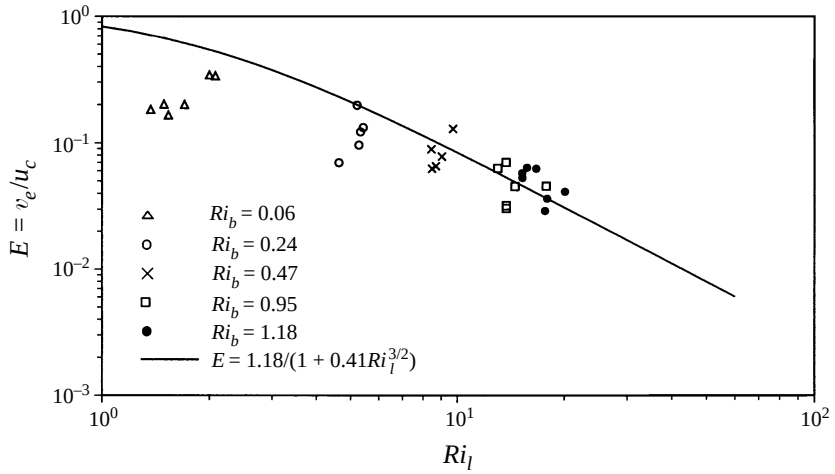

FIGURE 3. Variation of the entrainment constant with local Richardson number. The solid line represents the curve fit from Denton & Wood (1981) applied to the experimental data from Turner (1968).

The entrainment rate E should scale on local variables because it is determined by how much of the local turbulence is used for mixing. Depending on the strength of the stratification, various entrainment regimes may occur. Although there is currently disagreement regarding turbulent entrainment (Fernando 1991), it is accepted that

$$E = \frac{v_e}{u_c} = f(Ri_l) \sim Ri_l^m. \tag{4.2}$$

The characteristic velocity, u_c, is taken as the average vertical velocity in the interface and Ri_l is evaluated from quantities averaged over the interface. Local scaling has been found to collapse entrainment data fairly well (E & Hopfinger 1986).

In a simulation, the entrainment rate can be calculated at each instant. As the flow develops, Ri_l increases, mainly because the energy at the interface decreases due to increasing distance from the source. Similar values of Ri_l are found in simulations with different Ri_b. In figure 3, the instantaneous entrainment rate is shown for all the simulations. For $Ri_l < 5$, the entrainment rate appears to be independent of Ri_l. As we will see, the dominant entrainment mechanism in this range is large-scale engulfment. This result is supported by the experimental data of Fernando & Long (1985) and E & Hopfinger (1986).

For $Ri_l > 5$ the entrainment rate can be described by a power law with exponent $m \approx -1.5$ which is near the experimental values (E & Hopfinger 1986; Nokes 1988). The empirical relation

$$E = \frac{1.18}{1 + 0.41\, Ri_l^{3/2}}, \tag{4.3}$$

used by Denton & Wood (1981) to fit oscillating grid results from Turner (1968), is also shown in figure 3. The simulation and experimental data compare well for strong stratification. Entrainment for $Ri_l > 5$ is dominated by scouring mechanisms. The density interface quickly recovers from a large-eddy impact. The entrainment rate decreases because scouring is not as efficient as large-scale engulfment. Evidence of such turbulence structure is given in §5.4.

The scaling $E \sim Ri^{-1}$ can be derived by assuming that the rate of energy addition is proportional to the rate of change of the potential energy (Linden 1975). However, the rate of conversion of kinetic energy into potential energy at the interface is dependent on local quantities (such as the Froude number, which changes at the interface). Theoretical support for $m = -1.5$ was given by Linden (1973) using a model based on vortex ring penetration.

Experiments yield a wide variety of entrainment rate parameters (Fernando 1991). E & Hopfinger (1986) found $m = -3/2$, which agrees well with our results. Fernando & Long (1985) obtained $m = -7/4$. These two experiments span a range of Ri_l of at least two orders of magnitude. However, E & Hopfinger (1986) provide much more data with less scatter. Nokes (1988) measured the entrainment rate for a variety of grid configurations, strokes, and distances from the grid and found $m = -1.06$ to -1.43.

When the Richardson number is large enough the only entrainment mechanisms are molecular diffusion and internal wave breaking because turbulent motions are completely suppressed. For Ri_l larger than 10 ($Fr_v \leqslant 0.7$) the scalar transport continues to decrease because internal waves are created but do not contribute to the buoyancy flux. In this regime the power-law exponent may decrease (Fernando 1991). From the data in figure 3 it is difficult to determine whether the exponent changes. The experimental data that support $m = -7/4$ also contain a large amount of scatter (Fernando & Long 1985).

4.2. *Scale dependence of entrainment*

The discussion in §3.1 focused on the relative contributions of transport, buoyancy flux, and dissipation to the kinetic energy budget. Once the important terms are known, then spectra can reveal the contribution of various length scales to the mixing process at a stable interface. We shall look at the one-dimensional buoyancy flux spectrum

$$B(\kappa_x, y) = \sum_{\kappa_z} \hat{v}(\kappa_x, y, \kappa_z)\hat{\rho}^*(\kappa_x, y, \kappa_z) \tag{4.4}$$

which is easily constructed.

The velocity gradient tensor is defined in three-dimensional wave space:

$$\hat{s}_{ij}(\boldsymbol{k}) = \tfrac{1}{2}(k_j\hat{u}_i(\boldsymbol{k}) + k_i\hat{u}_j(\boldsymbol{k})). \tag{4.5}$$

This tensor is then transformed into (κ_x, y, κ_z)-space and used to define the dissipation spectrum. After summing over κ_z, we have a one-dimensional dissipation spectrum

$$D_{ij}(\kappa_x, y) = 2\nu \sum_{\kappa_z} \hat{s}_{im}(\kappa_x, y, \kappa_z)\hat{s}^*_{jm}(\kappa_x, y, \kappa_z). \tag{4.6}$$

One-dimensional spectra in the κ_z-direction formed by integrating over κ_x are statistically equivalent to these and can be used for averaging.

The spectral representation of turbulence transport and transfer appear in the evolution equation for the two-dimensional energy spectrum tensor,

$$E_{ij}(\kappa_x, y, \kappa_z) = \hat{u}_i(\kappa_x, y, \kappa_z)\ \hat{u}^*_j(\kappa_x, y, \kappa_z). \tag{4.7}$$

To derive the equation for this quantity the Fourier transform of the momentum

equation,

$$u_{\alpha,t} + u_k u_{\alpha,k} = -\frac{1}{\rho_o} p_{,\alpha} - \frac{g}{\rho_o} \rho \delta_{\alpha 2} + \nu u_{\alpha,kk}, \tag{4.8}$$

is taken in the two horizontal directions to produce

$$\frac{\partial \hat{u}_\alpha}{\partial t} + \mathscr{F}(u_k u_{\alpha,k}) = \mathscr{Z} \tag{4.9}$$

where $\mathscr{F}$ denotes a Fourier transform and $\mathscr{Z}$ represents the Fourier transform of the right-hand side of (4.8). Multiplying (4.9) by $\hat{u}_\alpha^*$ and adding it to the product of the complex conjugate of (4.9) and $\hat{u}_\alpha$ yields

$$\frac{\partial}{\partial t} \hat{u}_\alpha \hat{u}_\alpha{}^* + \hat{u}_\alpha \mathscr{F}^*(u_k u_{\alpha,k}) + \hat{u}_\alpha^* \mathscr{F}(u_k u_{\alpha,k}) = \hat{u}_\alpha^* \mathscr{Z} + \hat{u}_\alpha \mathscr{Z}^*. \tag{4.10}$$

The α indices are not summed over.

The second and third terms on the left-hand side of (4.10) represent the nonlinear transport of turbulence and can be split into two components. The first is the transport in the inhomogeneous direction:

$$H_{\alpha\alpha} = \hat{u}_\alpha \mathscr{F}^*(u_2 u_{\alpha,2}) + \hat{u}_\alpha^* \mathscr{F}(u_2 u_{\alpha,2}) + \tfrac{1}{2}\{\hat{u}_\alpha \mathscr{F}^*(u_\alpha u_{2,2}) + \hat{u}_\alpha^* \mathscr{F}(u_\alpha u_{2,2})\}. \tag{4.11}$$

The second, defined as

$$\begin{aligned} I_{\alpha\alpha} = {} & \hat{u}_\alpha \mathscr{F}^*(u_1 u_{\alpha,1}) + \hat{u}_\alpha^* \mathscr{F}(u_1 u_{\alpha,1}) + \hat{u}_\alpha \mathscr{F}^*(u_3 u_{\alpha,3}) + \hat{u}_\alpha^* \mathscr{F}(u_3 u_{\alpha,3}) \\ & - \tfrac{1}{2}\{\hat{u}_\alpha \mathscr{F}^*(u_\alpha u_{2,2}) + \hat{u}_\alpha^* \mathscr{F}(u_\alpha u_{2,2})\}, \end{aligned} \tag{4.12}$$

represents the spectral transfer of energy among wavenumbers within a horizontal plane.

The one-dimensional spectra of the transport and transfer spectra are defined as

$$H_{\alpha\alpha}(\kappa_x, y) = \sum_{\kappa_z} H_{\alpha\alpha}(\kappa_x, y, \kappa_z) \tag{4.13}$$

and

$$I_{\alpha\alpha}(\kappa_x, y) = \sum_{\kappa_z} I_{\alpha\alpha}(\kappa_x, y, \kappa_z), \tag{4.14}$$

respectively. The form of $H_{\alpha\alpha}$ is chosen such that the sum over all horizontal wave numbers yields the average turbulence transport in a horizontal plane. That is,

$$\sum_{\kappa_x} H_{\alpha\alpha}(\kappa_x, y) = \frac{\partial}{\partial y} \overline{u_\alpha u_\alpha v}(y). \tag{4.15}$$

Similarly, summing $I_{\alpha\alpha}(\kappa_x, y)$ over κ_z yields

$$\sum_{\kappa_x} I_{\alpha\alpha}(\kappa_x, y) = 0, \tag{4.16}$$

which shows that $I_{\alpha\alpha}$ represents transfer and does not contribute to the overall energy balance.

In figure 4(*a*), transport spectra, H_{22}, are shown for $Ri_b = 0.24$, 0.47, and 1.18 at $y^* = 0.5$. This is the approximate location of maximum transport in all simulations (see figure 2*a–c*). The transport is negative and concentrated at low wavenumbers, indicating that the large scales are responsible for most of the energy transport which is an energy loss in this region. The curves in figure 4(*a*) are noisy due to the limited

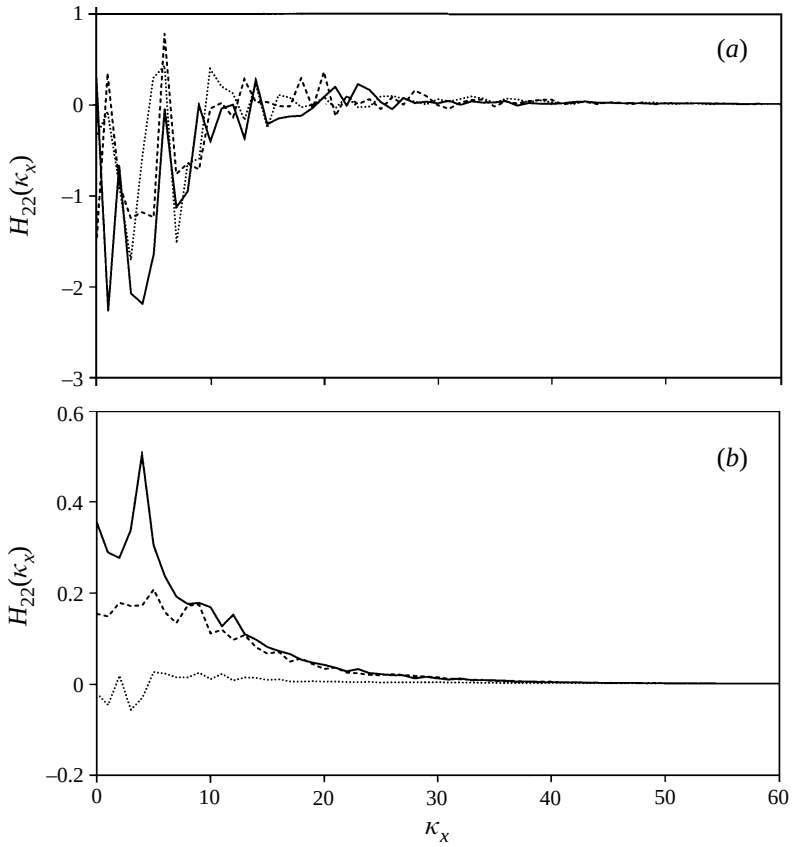

FIGURE 4. Transport spectra of the vertical velocity component at $t^* = 10.6$, and (*a*) $y^* = (y - y_s)/l_s = 0.5$, (*b*) $y^* = 1.7$. ——, $Ri_b = 0.24$; – – – –, $Ri_b = 0.47$; (· · · ·), $Ri_b = 1.18$.

sample size. The transport at $y^* = 1.7$, shown in figure 4(*b*) for the same cases, is positive in the large scales, indicating that the large scales receive energy in this region (through transport by the turbulence above). As Ri_b increases, less energy is received because stable stratification prevents the penetration of large scales. Energy is also removed from large scales and diverted into buoyancy flux.

In figure 5(*a–c*) contours of the transport are shown for $Ri_b = 0.24, 0.47$, and 1.18, respectively. For clarity, only contours of positive transport (receiving energy) are shown. The full range of wavenumber (κ_x) and distance from the source (y^*) is displayed. Near the source, there is little positive transport: positive transport is generally found at $y^* > 1$. As the stratification strengthens, the large scales become less capable of transporting energy; consequently the contours do not extend as far from the source. In the $Ri_b = 1.18$ case, the contours furthest from the source are more closely spaced than in the $Ri_b = 0.24$ simulation, indicating that the interface sharply reduces transport and acts as a barrier.

Figure 6(*a,b*) shows the transfer spectra, I_{22}, for the same Ri_b at $y^* = 0.5$ and $y^* = 1.7$, respectively; they integrate to zero in each horizontal plane. Near the source, the cascade of energy is evident: large scales transfer energy to small scales. No effects of stratification are present at this location. At $y^* = 1.7$, the spectral transfer process is not active, even in the weakly stratified case in which a relatively

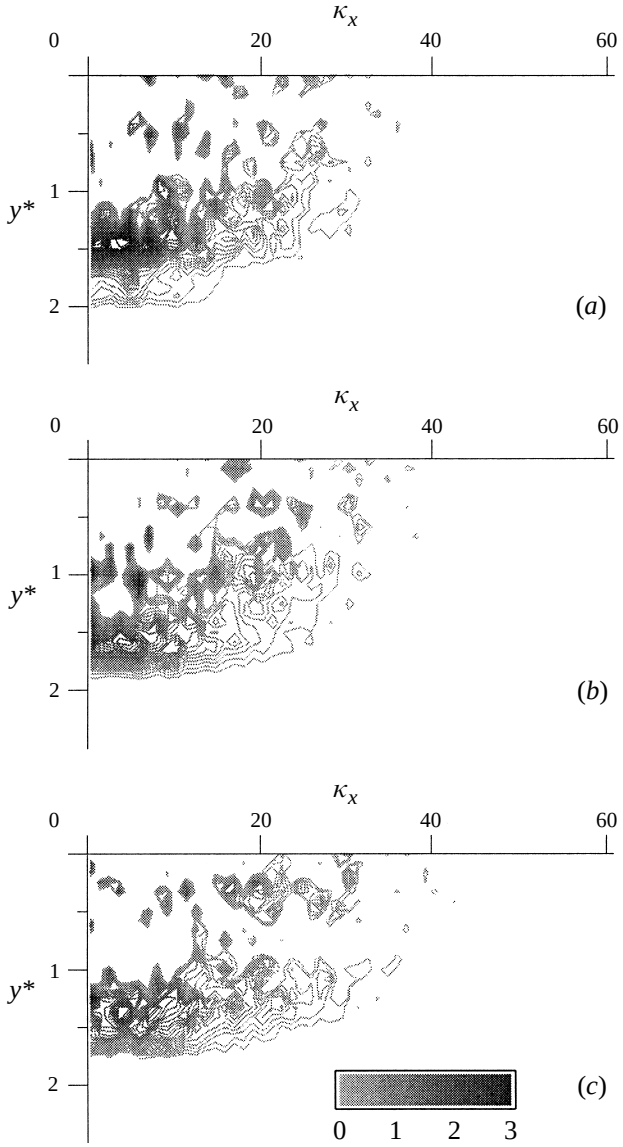

FIGURE 5. Contours of positive transport (H_{22}) at $t^* = 10.6$. Contour levels are identical in each plot and normalized by the source intensity at $y^* = 0$.

large amount of energy is transported. Although some transfer from the small to large scales (reverse cascade) occurs, its magnitude is extremely small (note the change of scale in figure 6*b*) so the energy remains in the large scales. Apparently, stratification has weakened the turbulence and disrupted the transfer of energy.

The large and medium scales contribute to the dissipation near the source, at $y^* = 0.5$. Figure 7(*a*) shows the dissipation spectra at this location for $Ri_b = 0.24$, 0.47, and 1.18. The scale corresponding to the peak of $D_{22}(\kappa_x)$ is approximately ten times the Kolmogorov scale. At $y^* = 1.7$ only the large scales dissipate energy (figure 7*b*) and energy is transported by the large scales. Without active spectral transfer, energy can only be dissipated at the large scales or converted into buoyancy flux

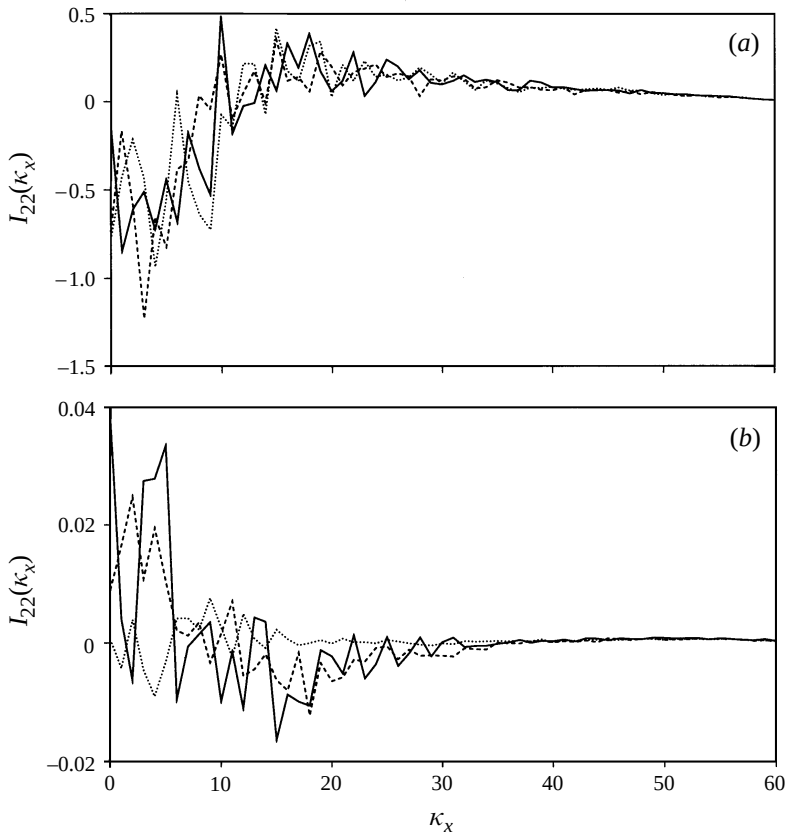

FIGURE 6. Transfer spectra of the vertical velocity component at $t^* = 10.6$, and (*a*) $y^* = (y - y_s)/l_s = 0.5$, (*b*) $y^* = 1.7$. ——, $Ri_b = 0.24$; – – – –, $Ri_b = 0.47$; · · · ·, $Ri_b = 1.18$.

or internal waves. In the highly stratified flow ($Ri_b = 1.18$), the dissipation is much smaller at $y^* = 1.7$ because few large scales are able to penetrate to this depth. Also, more energy is diverted into buoyancy flux.

4.3. *The scale of buoyancy flux*

Buoyancy flux spectra at $y^* = 0.5$ are shown in figure 8(*a*). In all cases the buoyancy flux is confined to the large scales and is positive, indicating down-gradient mixing. Although the density gradient in this region is weak, the turbulence receives energy from the source and some mixing occurs.

As the distance from the source increases to $y^* = 1.7$, the large-scale buoyancy flux remains down-gradient (actively mixing) as shown in figure 8(*b*). The flux is weaker due to the reduced available kinetic energy and the presence of internal waves, which do not contribute to buoyancy flux. The spectra are noisy because there are few large-scale eddies. Without an active energy cascade, the down-gradient flux must occur at the largest scales because the turbulence is active only at low wavenumbers.

Most of the stirring is accomplished by the large scales. However, at the medium to small scales, very weak counter-gradient fluxes occur. Three contour plots of the counter-gradient buoyancy flux are shown in figure 9(*a–c*), for $Ri_b = 0.24$, 0.47, and

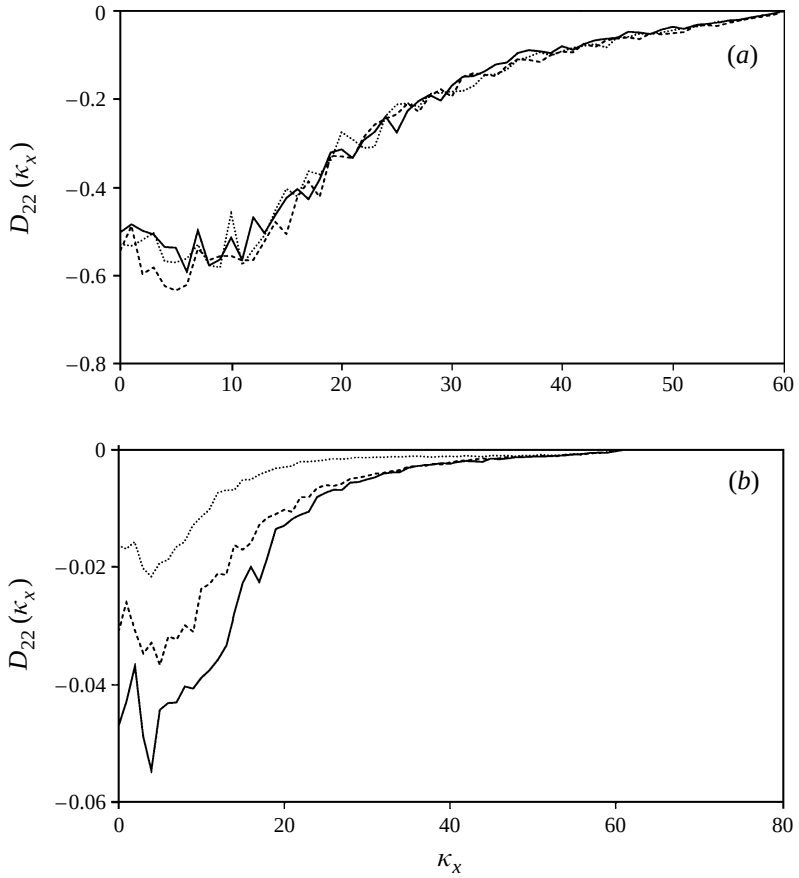

FIGURE 7. Dissipation spectra of the vertical velocity component at $t^* = 10.6$, and (*a*) $y^* = (y - y_s)/l_s = 0.5$, (*b*) $y^* = 1.7$. ——, $Ri_b = 0.24$; – – – –, $Ri_b = 0.47$; · · · ·, $Ri_b = 1.18$.

1.18, respectively. The contours represent the scales at which heavy (light) fluid is descending (ascending) and restratifying. The contours are far from the source and at medium to small wavenumbers. As stratification increases, a wider range of scales become counter-gradient and they are confined to a thinner vertical layer. However, these motions are much less energetic than the down-gradient fluxes occurring at the large scales (compare contour levels to down-gradient flux magnitudes in figure 8). The homogeneous turbulence simulations of Holt *et al.* (1992) also produced counter-gradient fluxes at the largest wavenumbers for sufficiently large *Ri*. In the absence of turbulence transport and spectral transfer these scales receive energy by the transfer of potential energy to kinetic energy in the restratification process.

In addition to Reynolds number, the appearance and scale of counter-gradient fluxes may depend on N and Pr (Itsweire & Helland 1989; Holt *et al.* 1992). The unsheared linearly stratified experiments of Lienhard & Van Atta (1990) at $N = 2.42\ \mathrm{s}^{-1}$, $Pr = 0.7$, showed that large scales are crushed by buoyancy forces and eventually become counter-gradient while the smallest scales continue to mix. Data from Itsweire & Helland (1989), recorded at lower buoyancy frequency and $Pr \gg 1$, show that energy is suppressed by stratification in all scales without counter-gradient fluxes.

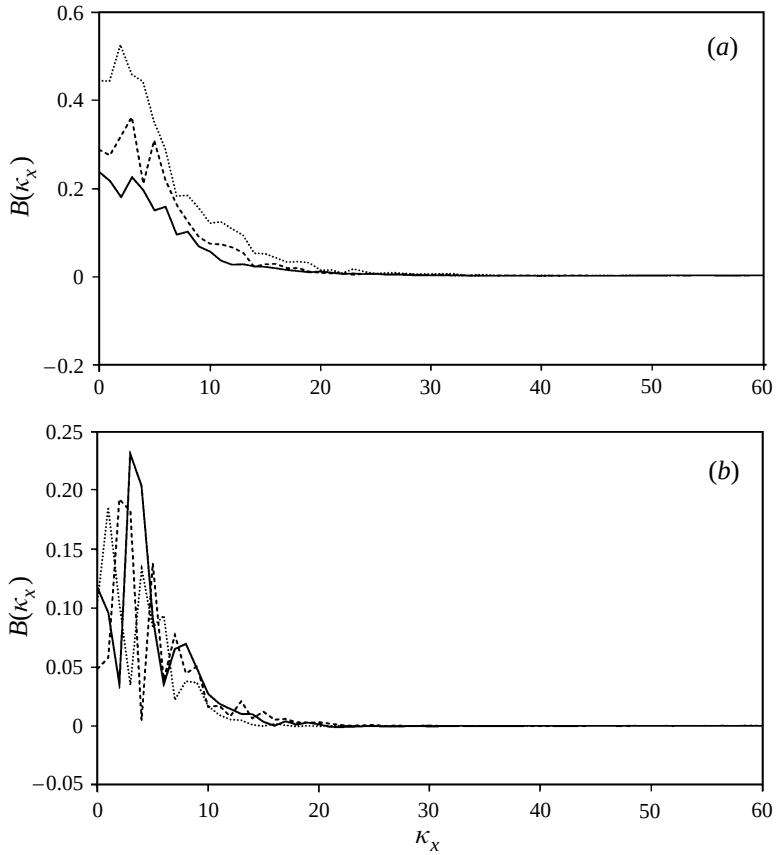

FIGURE 8. Buoyancy flux spectra at $t^* = 10.6$, and (*a*) $y^* = (y - y_s)/l_s = 0.5$, (*b*) $y^* = 1.7$. ——, $Ri_b = 0.24$; – – – –, $Ri_b = 0.47$; · · · ·, $Ri_b = 1.18$.

4.4. *Interruption of the energy cascade*

The interruption of the cascade can be analysed using energy spectra at various locations in the mixing layer. The one-dimensional energy spectrum is defined as

$$E_{ij}(\kappa_x, y) = \sum_{\kappa_z} E_{ij}(\kappa_x, y, \kappa_z). \tag{4.17}$$

In figure 10(*a*), one-dimensional spectra of the vertical energy are shown at $y^* = 1.5$ for $Ri_b = 0.0$, 0.24, and 1.18. The total energy is lower in the high-Ri_b cases due to reduced energy transport. Figure 10(*b*) shows the energy spectra at $y^* = 1.75$ for the same simulations. All of the spectra are less energetic than at $y^* = 1.5$, owing to increased distance from the source. Owing to the low energy level, even the unstratified spectrum at $y^* = 1.75$ may not support an energy cascade (energy decays as approximately $k \sim y^{-2.45}$ in the simulations and as $k \sim y^{-2.0}$ in most experiments, Hannoun *et al.* 1988). Stratification further reduces the energy level (see §5.4).

The first effect of stratification appears in the large scales: with less available energy, large-scale overturns are reduced or prevented entirely. Without active overturning, the medium scales lose their primary source of energy in the interface region, as evidenced by the spectra. Some energy is generated in the medium scales

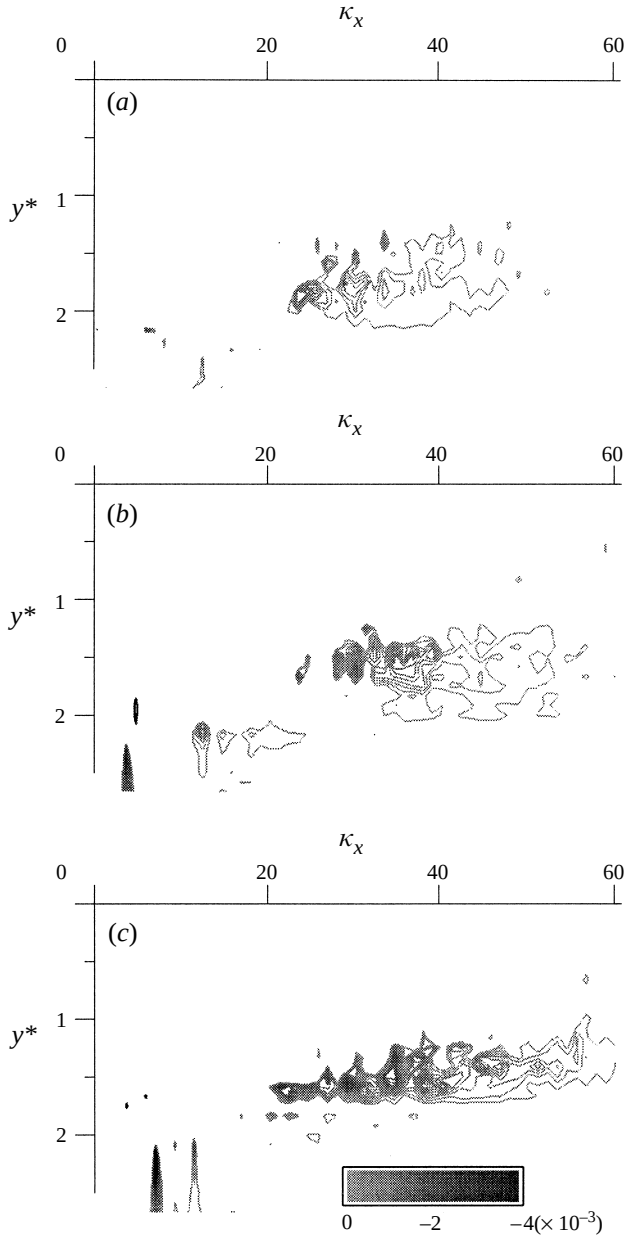

FIGURE 9. Contours of counter-gradient buoyancy flux at $t^* = 10.6$ for various Richardson numbers. Contour levels are identical for each plot and normalized by the buoyancy flux at $y^* = 0$.

by the source but these eddies never reach the interface unless carried there by a larger eddy. Although the energy in the large scales decreases with distance from the source, these eddies remain energetic enough to deform the interface. After a large eddy penetrates the interface, diffusion tends to smooth it and only a small core retains enough buoyancy to allow conversion of potential energy to kinetic energy.

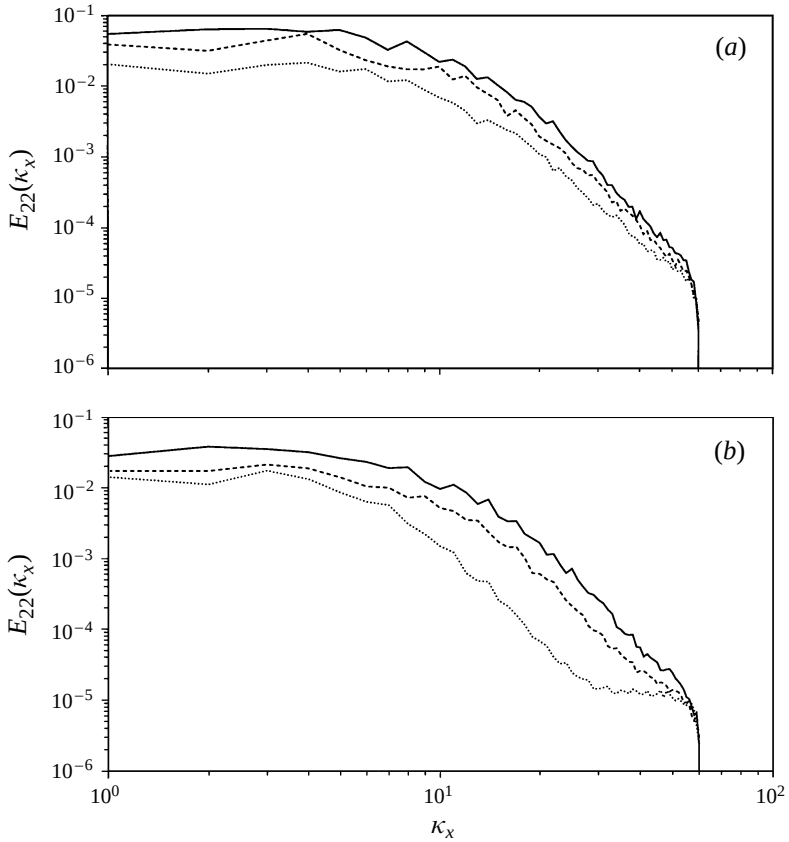

FIGURE 10. One-dimensional vertical energy spectra at (*a*) $y^* = (y - y_s)/l_s = 1.5$ and (*b*) $y^* = 1.75$, at $t^* = 10.6$. ——, $Ri_b = 0.24$; – – – – –, $Ri_b = 0.47$; · · · ·, $Ri_b = 1.18$.

5. Correlation with turbulent Froude number

The previous sections presented results with respect to y^*. We shall see that the vertical turbulent Froude number Fr_v (equation (2.7)) is the best parameter for the local state of the turbulence under stable stratification. In figure 11, profiles of Fr_v are shown for $Ri_b = 0.24$, 0.47, and 1.18 at $t^* = 10.6$. The Froude number is large in the source region because the density gradients are small and the turbulence is energetic. As the interface is approached, Fr_v decreases as the density gradient increases and turbulence energy decays. The vertical turbulent Froude number reaches a minimum value of about 0.7, independent of Ri_b. This occurs near the centre of the interface where the time scales of the turbulence and buoyancy are nearly equal. A minimum Fr_v is reached because the turbulence cannot overturn when its time scale is shorter than the buoyancy time scale. Although the curves are similar, the minimum value of Fr_v occurs closer to the source as stratification increases because buoyancy slows the propagation of the turbulence.

5.1. *Mixing efficiency*

Mixing in stratified turbulent flows is quantified by the down-gradient buoyancy flux. The efficiency with which kinetic energy is converted into buoyancy flux is central to many models (Linden 1975) and scales with the vertical turbulent Froude number. The mixing efficiency, η, is defined as the ratio of buoyancy flux to the energy available for

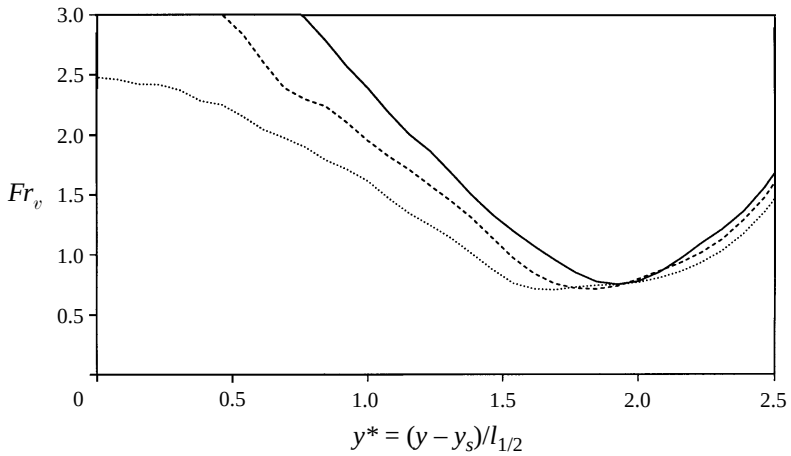

FIGURE 11. Profiles of the vertical turbulent Froude number at $t^* = 10.6$: ——, $Ri_b = 0.24$; – – – – –, $Ri_b = 0.47$; · · · ·, $Ri_b = 1.18$.

mixing (Ivey & Imberger 1991). For shear-free inhomogeneous turbulence the mixing efficiency is

$$\eta = \frac{B}{T + S_k} \tag{5.1}$$

where B is the buoyancy flux and T and S_k denote the contributions from the transport and the source, respectively (T refers to the first two terms on the right-hand side of equation (2.1)). Winters *et al.* (1995) defined a mixing efficiency in terms of an irreversible mixing rate to eliminate ambiguity when internal waves and counter-gradient fluxes are present.

Using (2.1) and assuming steady conditions and negligible molecular diffusion, (5.1) can be recast as

$$\eta = \frac{B}{B + \epsilon} \tag{5.2}$$

where $B = g\overline{v\rho}/\rho_o$ and $\epsilon = \nu\overline{u_{i,k}u_{i,k}}$. Under weak stratification ($Fr_v \gg 1$), the mixing efficiency is nearly zero because the turbulence vigorously mixes fluid of nearly constant density. Little buoyancy flux is produced and most of the energy is dissipated. The mixing efficiency under strongly stratified conditions ($Fr_v < 1$) is also nearly zero because most turbulent eddies are unable to stir the fluid. Furthermore, fluid that is stirred by the strongest eddies may not mix owing to the production of counter-gradient fluxes and/or internal waves.

In figure 12, the mixing efficiency is plotted against the isotropic Froude number, Fr_t, a parameterization suggested by Ivey & Imberger (1991). Values from two homogeneous stratified turbulent flows are also shown – the linearly stratified sheared simulations of Holt *et al.* (1992) at $Re_\lambda = 52$ and the linearly stratified unsheared experiments of Lienhard & Van Atta (1990) at $Re_\lambda \approx 30$. The data show similar trends, although the peak mixing efficiency and corresponding isotropic Froude number differ. The three data sets represent fundamentally different stratified turbulent flows that evolve from isotropic initial conditions to different anisotropic states.

The anisotropy of these flows as a function of Fr_t is shown in figure 13. The turbulent Froude number decays with time in the homogeneous flows because N is

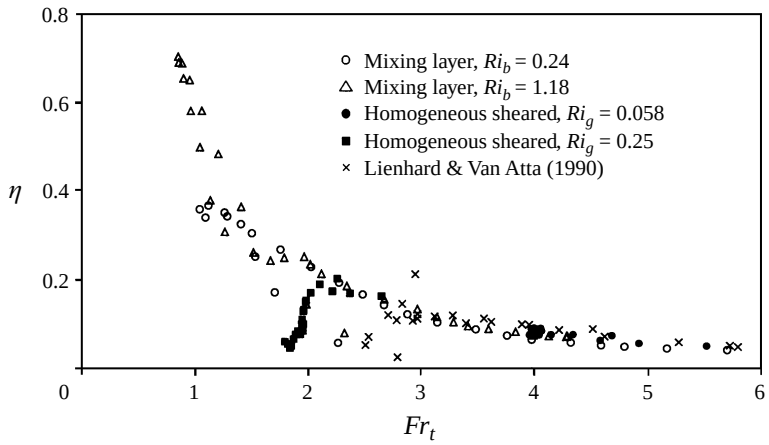

FIGURE 12. Mixing efficiency as a function of isotropic Froude number, Fr_t, for the mixing layer, homogeneous sheared simulations of Holt *et al.* (1992), and unsheared experiments of Lienhard & Van Atta (1990).

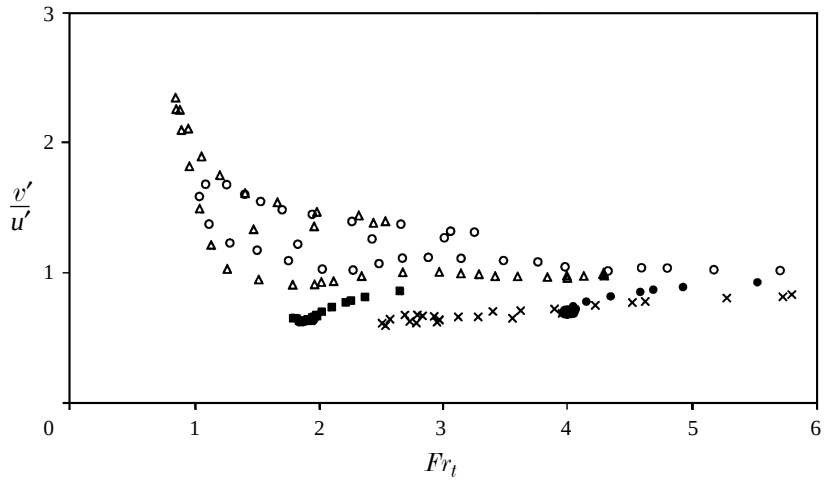

FIGURE 13. Development of the anisotropy as a function of Fr_t. u' represents the average horizontal velocity in the inhomogeneous flows and the spanwise velocity in the homogeneous flows. Symbols as figure 12.

fixed and v' decreases. (Although the shear in the weakly stratified case of Holt *et al.* 1992 was strong enough to increase q, the Ellison scale grew faster causing Fr_t to decay.) In these flows, the vertical r.m.s. velocity is attenuated, causing $v'/u' < 1$. For the cases with mean shear, u' is taken as the spanwise component because mean shear increases the r.m.s. velocity in the streamwise direction (Holt *et al.* 1992). Our mixing layer simulations are quasi-steady (for $Ri_b > 0$ the density field affects the velocity field slightly) and evolve with distance from the source; the turbulent Froude number decays with y^*. The eddies that penetrate the interface (marked by $Fr_v < 1.5$) have $v'/u' > 1$ because they require a large amount of vertical kinetic energy to reach the interface. For $Ri_b = 1.18$, the eddies flatten at the top of the interface ($1.5 < Fr_v < 2.0$) causing v'/u' to drop below unity. As shown above, the peak mixing efficiency in the inhomogeneous simulations is higher than in the homogeneous flows, because, in the

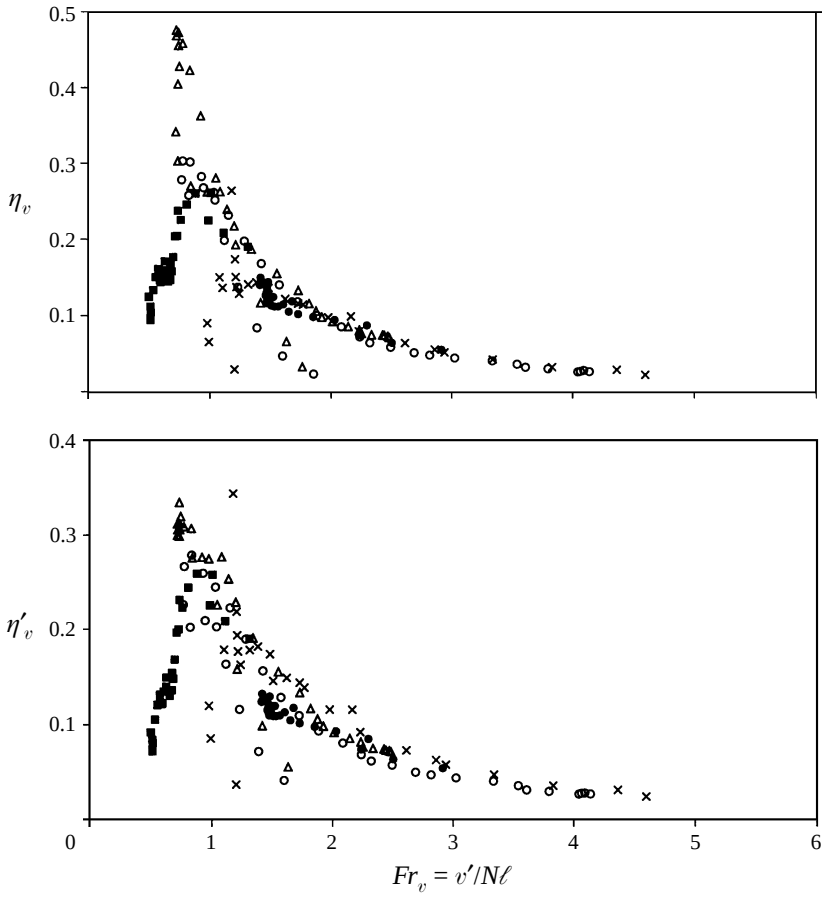

FIGURE 14. Vertical mixing efficiencies (*a*) η_v and (*b*) η'_v as a function of vertical Froude number, Fr_v. Symbols as figure 12.

interface region, v'/u' is larger in these flows. The horizontal components of energy do not directly contribute to buoyancy flux.

By incorporating the anisotropy into the Froude number and mixing efficiency, a better collapse of the data can be obtained. The vertical turbulent Froude number is a more appropriate parameter because it is based on the vertical velocity, the component responsible for mixing. In figure 14(*a*), the vertical mixing efficiency, defined as

$$\eta_v = \left(\frac{q}{\sqrt{3}v'}\right)\eta, \tag{5.3}$$

is plotted against vertical turbulent Froude number and the data collapse markedly improves. The maximum mixing efficiency occurs at $Fr_v \approx 1$.

To further emphasize the anisotropy of the turbulence, an alternative vertical mixing efficiency is defined as

$$\eta'_v = \left(\frac{u'}{v'}\right)\eta. \tag{5.4}$$

Use of this parameter is suggested by the kinds of arguments given in Briggs *et al.* (1996). With this definition, the peak mixing efficiency is approximately 0.3 for

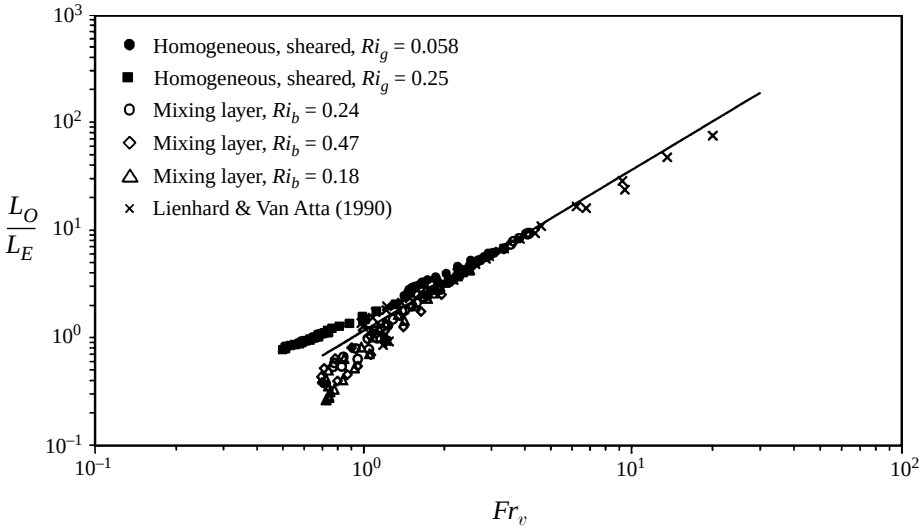

FIGURE 15. Ratio of the Ozmidov scale to the Ellison scale for a range of vertical Froude numbers.

inhomogeneous flows, as shown in figure 14(*b*). The peak isotropic mixing efficiencies (η) are about 0.25 (Ivey *et al.* 1992), as shown in figure 12. The vertical mixing efficiency is expected to be larger. Both definitions of vertical mixing efficiency reduce to η in isotropic turbulence. Note that the overall efficiency of converting source energy into potential energy is much lower than the mixing efficiency because most of the energy is dissipated before it reaches the interface region.

Two other conclusions can be reached relative to the turbulent Froude number. First, models for the deepening of the mixed layer and entrainment rate assume a constant rate of conversion of turbulence energy into potential energy. These can be improved by using the dependence of η_v' on Fr_v. Secondly, it is interesting that the mixing efficiency in all of the flows evolves toward a state of maximum mixing efficiency. After this maximum is reached, however, $\overline{v\rho}$ and η_v rapidly decrease owing to internal wave and counter-gradient flux production.

5.2. *Length scales in inhomogeneous stratified turbulence*

The Ozmidov scale, defined as

$$L_O = \left(\frac{\epsilon}{N^3}\right)^{1/2}, \tag{5.5}$$

represents the largest possible overturning scale in a stratified flow (Ozmidov 1965). Turbulence scales larger than L_O are dominated by buoyancy and do not possess enough kinetic energy to overturn. To calculate the Ozmidov scale from experimental data, the dissipation is typically estimated using components of the strain rate tensor. A review of many dissipation models is given in Itsweire *et al.* (1992).

The results from stably stratified experiments (Itsweire, Helland & Van Atta 1986; Rohr *et al.* 1988) and simulations (Itsweire *et al.* 1992) indicate that stratification begins to dominate the turbulence when the overturning scale (2.6) and the Ozmidov scale are approximately equal. To examine the onset of buoyancy-controlled turbulence, the Froude-number dependence of the ratio L_O/L_E is shown in figure 15. Data from the homogeneous sheared simulations of Holt *et al.* (1992) and homogeneous unsheared experiments of Lienhard & Van Atta (1990) are included for comparison.

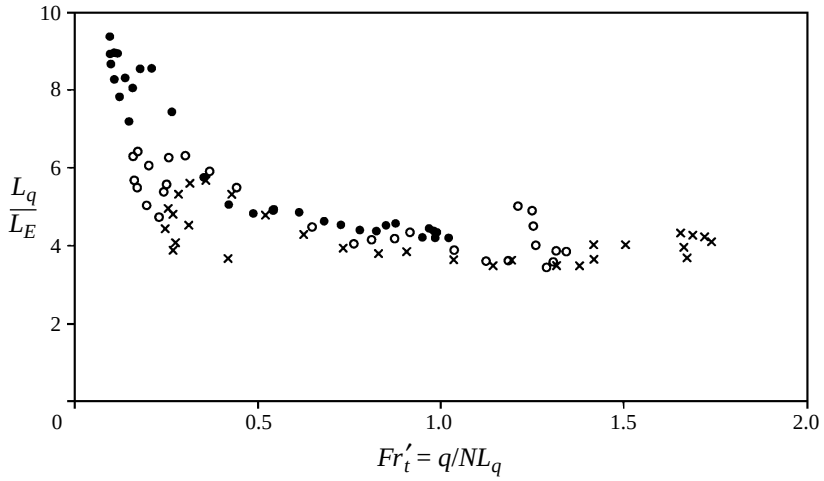

FIGURE 16. Ratio of the integral scale to the Ellison scale for a range of Fr_t'. Symbols as figure 12.

For $Fr_v > 1$ data from all flows collapse well and approach

$$\frac{L_O}{L_E} \sim Fr_v^{3/2} \tag{5.6}$$

at higher Fr_v. Ivey & Imberger (1991) originally derived this relationship in terms of Fr_t; however for highly energetic turbulence $Fr_v \sim Fr_t$. When $Fr_v \approx 1$, buoyancy significantly influences the evolution of the turbulence and the two scales are nearly equal. Itsweire *et al.* (1992) find that $L_O \approx L_E$ in stratified shear flow when the turbulence production is in balance with the dissipation and buoyancy flux (the stationary Richardson number condition).

For $Fr_v < 1$, L_O/L_E can be less than unity even though L_O is theoretically the largest scale in a stratified flow. This is caused by internal waves which contribute to the Ellison scale but not to the Ozmidov scale (Itsweire *et al.* 1992). The internal wave field may be more active in the inhomogeneous unsheared simulations when stratification is significant ($Fr_v < 1$). As a result, L_O/L_E is smaller in the inhomogeneous flows for low Fr_v.

An estimate of the integral length scale,

$$L_q = \frac{q^3}{\epsilon}, \tag{5.7}$$

should be proportional to the Ellison scale in weakly stratified turbulence because both scales characterize the largest scales. If this relationship is known, the integral scale can be used as a surrogate for the Ellison scale, which can be difficult to measure. The ratio of L_q to L_E as a function of $Fr_t' = q/NL_q$ is shown in figure 16. For $Fr_t' > 0.5$, L_q/L_E is approximately 4. As the interface is approached, L_q/L_E increases and becomes dependent on Fr_t'. The Ellison scale decreases rapidly as the stratification intensifies because the large scales are too weak to create large fluctuations in the density field. However, under weakly stratified conditions, the Ellison scale can be accurately obtained from the estimate of the integral scale, L_q.

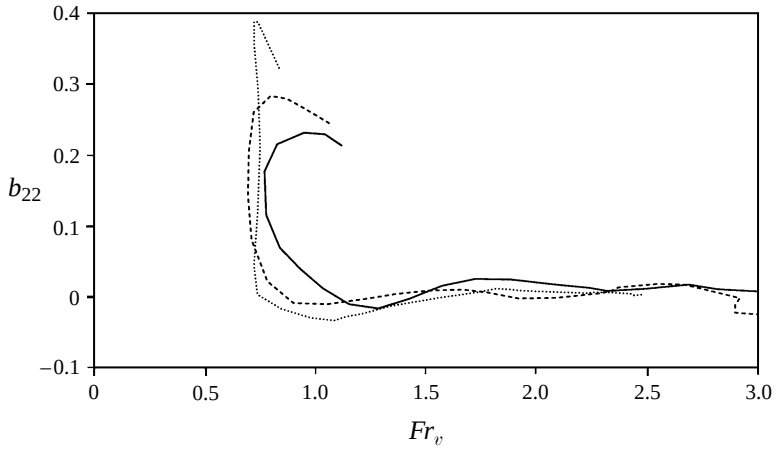

FIGURE 17. Dependence of anisotropy ratio, b_{22}, on vertical Froude number ($t^* = 10.6$): ——, $Ri_b = 0.24$; – – – –, $Ri_b = 0.47$; · · · ·, $Ri_b = 1.18$.

5.3. *Large-scale anisotropy*

As discussed above, the anisotropy of the large scales, which is quantified by the anisotropy tensor

$$b_{ij} = \frac{\overline{u_i u_j}}{q^2} - \frac{\delta_{ij}}{3}, \tag{5.8}$$

can be used to interpret the state of the turbulence. In figure 17, b_{22} is shown for $Ri_b = 0.24, 0.47$, and 1.18. In all the simulations, b_{22} is approximately zero for $Fr_v \gg 1$ because the forcing is isotropic. As the interface is approached ($Fr_v \to 1$), b_{22} becomes slightly negative. The effect becomes more pronounced as Ri_b increases. This indicates that the eddies are flattened upon reaching the interface. Hannoun *et al.* (1988) show energy spectra which support the flattening effect. For $Fr_v < 1$, b_{22} increases and becomes positive because the energy in the eddies that are strong enough to penetrate the interface, where N decreases, contain mostly vertical kinetic energy. This energy is converted into buoyancy flux and dissipation and not into horizontal kinetic energy through flattening. Consideration of the horizontal anisotropy is not necessary because $b_{11} = b_{33} = -b_{22}/2$.

5.4. *Classification of turbulence structure*

Although the turbulence structure depends on the Richardson number, two regimes with distinct structure can be distinguished. Under buoyancy affected, or weakly stratified, conditions entrainment is accomplished by engulfment. Without strong buoyancy forces large eddies are able to overturn and transport fluid of different density over large distances. When buoyancy dominates, the interface becomes a barrier to turbulence, dramatically slowing the mixing rate.

To examine the deformation of the interface, a surface of constant density (isopycnal) is shown in figure 18(*a*) for $Ri_b = 0.24$. This density surface corresponds to $y^* \approx 1.7$ and $Fr_v > 1$. For reference, the complete range of density is shown in two planes perpendicular to the interface. The stirring mechanisms in weakly stratified turbulence are associated with eddies of the integral scale ($q^{3/2}/\epsilon$); their time scale is shorter than the buoyancy time scale ($Fr_v > 1$). Consequently, the large scales have enough time to penetrate the interface region and overturn be-

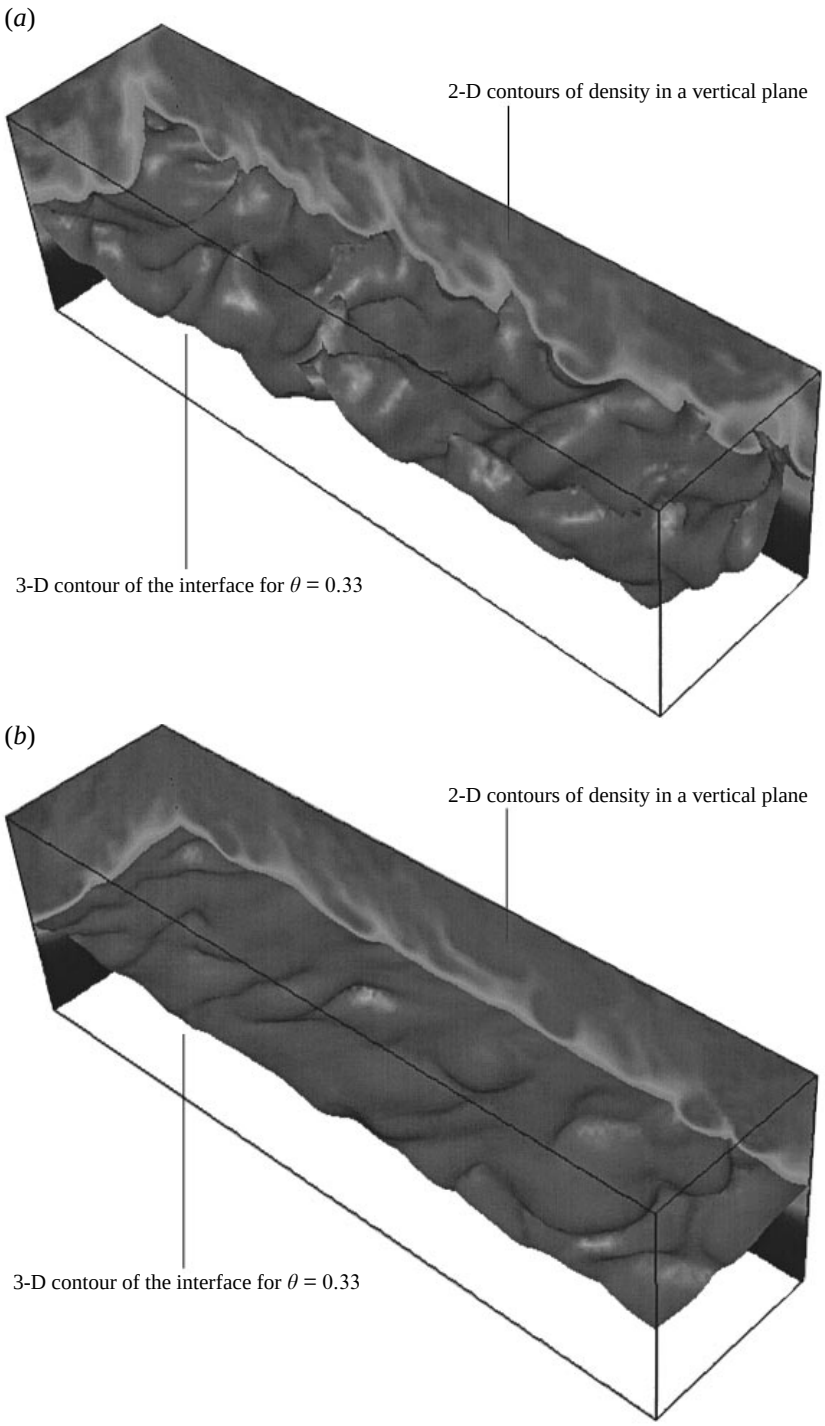

FIGURE 18. Two- and three-dimesional views of the density field at $t^* = 10.6$ and $y^* \approx 1.7$: (*a*) $Fr_v \approx 1$, $Ri_b = 0.24$, (*b*)$Fr_v \approx 0.7$, $Ri_b = 1.18$.

fore buoyancy can exert its influence. However, density perturbations are relatively small under weakly stratified conditions and little buoyancy flux is produced. Molecular mixing can occur once the large-scale stirring increases the local density gradients. Using shadowgraphs, Turner (1968) found similar mechanisms. The impact of large structures and the resulting engulfment can be seen at the interface. The transport of interface fluid into the mixed layer (where it is subsequently mixed) is visible in the two-dimensional contours. This two-stage mixing mechanism is similar to the wave-breaking mechanism described by De Silva & Fernando (1992).

A constant-density surface for $Ri_b = 1.18$ is shown in figure 18(b). This surface is also located at $y^* \approx 1.7$; however $Fr_v < 1$ at this location. The interface and the contours are relatively undisturbed indicating that transport into the mixed layer is much slower. The scouring mechanism becomes active when the stratification is strong enough to cause large eddies to flatten at the interface. In this process the vortical motions scour the interface and move small amounts of fluid upward. Figure 18(b) contains several examples of eddy flattening. Fluid that has been scoured from the interface is visible in the two-dimensional contours. Visualization of the interface in laboratory experiments also reveals the presence of scouring (Fernando & Long 1985). The anisotropy of the turbulence supports these results (see §5.3). Rebounding and internal wave breaking can also occur under strong stratification (Fernando 1991; Breidenthal 1992; Linden 1973). However, rebounding events, which happen when the eddy descends below the level of neutral buoyancy and then recoils due to the buoyancy force, were not observed in the present simulations and may be absent at low Re_λ. We also see little evidence of internal wave breaking as proposed by H. J. S. Fernando (1996, personal communication); that may be due to the fact that their theory assumes values of the Richardson and Reynolds numbers that are much larger than those in our simulations.

Another noticeable feature of figure 18(b) is the absence of small-scale disturbances on the interface. The deformation of the surface is caused almost exclusively by large eddies because small eddies are not energetic enough to reach or deform the interface. This behaviour is supported by the spatial dependence of the integral length scale in shear-free inhomogeneous turbulence, which increases with distance from the source (Hopfinger & Toly 1976). Turbulence structure at the density interface in the buoyancy affected simulation ($Ri_b = 0.24$) is very different from that in a buoyancy dominated one ($Ri_b = 1.18$).

5.5. *Estimating the buoyancy flux*

When diffusion is negligible, buoyancy flux is primarily responsible for changes in the mean density field. Although direct measurement of $\overline{v\rho}$ is possible in field studies (Imberger & Head 1994), it is difficult to obtain and is typically inferred from other data. The buoyancy flux can be estimated from limited measurements by taking advantage of the constancy of the correlation coefficient $R_{v\rho} = \overline{v\rho}/v'\rho'$ at large Fr_v ($R_{v\rho}$ is approximately 0.6 for $Fr_v \gg 1$, Ivey & Imberger 1991). An eddy viscosity model for the flux $\overline{v\rho}$ is

$$\overline{v\rho} = R_{v\rho}\, v'\, \rho' \approx -R_{v\rho}\, v'\, L_E \frac{\partial \overline{\rho}}{\partial y} \tag{5.9}$$

and is based on a turbulence velocity scale, an overturning scale, and the mean density. For weakly stratified flows, the Ellison scale is proportional to L_q (see §5.2). Using

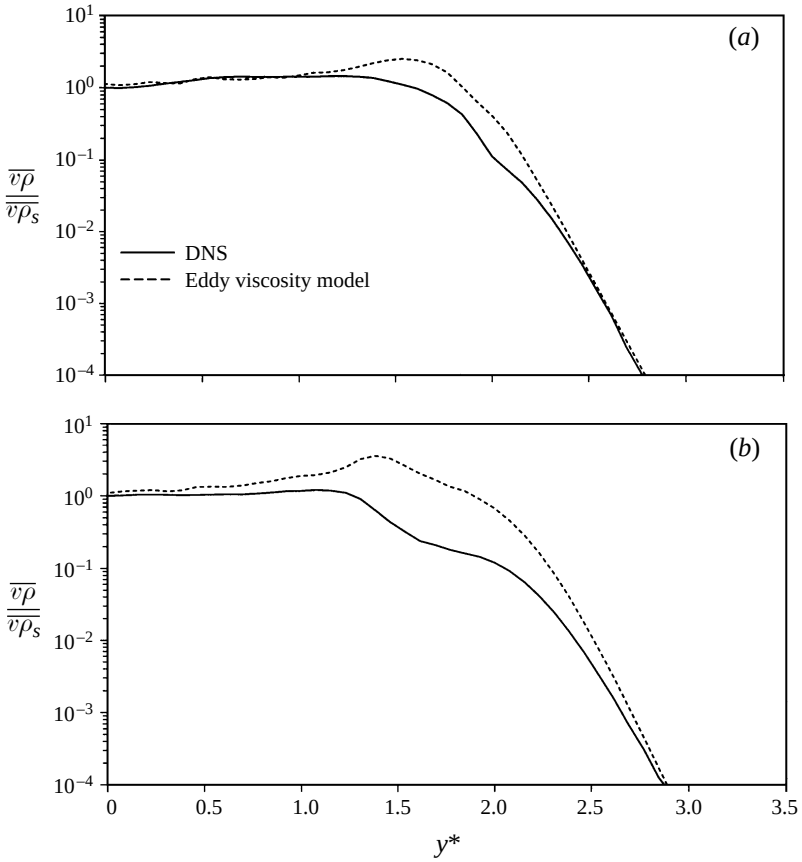

FIGURE 19. Normalized buoyancy flux and model given by equation (5.10) for $Ri_b = 0.24$, $t^* = 10.6$. Quantities are normalized by $\overline{v\rho}$ at $y^* = 0$. (*a*) $Ri_b = 0.24$, (*b*) $Ri_b = 1.18$.

the integral scale, L_q, the flux for weakly stratified cases can be approximated as

$$\overline{v\rho} \approx -R_{v\rho}\ v'\ (L_q/4)\frac{\partial \overline{\rho}}{\partial y}. \tag{5.10}$$

Predictions based on (5.10) for $Ri_b = 0.24$ and $Ri_b = 1.18$ are shown in figure 19(*a,b*). For the weakly stratified case, the model performs well throughout the layer but gives values that are high near the interface ($1.5 < y^* < 2$ and $Fr_v \approx 1$). At this location, internal waves and counter-gradient fluxes reduce $R_{v\rho}$, which is assumed constant in (5.10). In the $Ri_b = 1.18$ simulation, the Froude numbers are smaller and the predictions produced by (5.10) are less accurate.

6. Internal waves generated by turbulence

Two types of one-dimensional spectra involving the vertical velocity and density fluctuations are helpful in the identification of internal waves (Piccirillo 1993). The first is the co-spectrum, defined as

$$Co_{v\rho}(\kappa_x, y) = \mathrm{Re}\left\{\sum_{\kappa_z} \hat{v}(\kappa_x, y, \kappa_z)\ \hat{\rho}^*(\kappa_x, y, \kappa_z)\right\}, \tag{6.1}$$

and the second is the quadrature spectrum, defined as

$$Qu_{v\rho}(\kappa_x, y) = \mathrm{Im}\left\{\sum_{\kappa_z} \hat{v}(\kappa_x, y, \kappa_z)\ \hat{\rho}^*(\kappa_x, y, \kappa_z)\right\}. \tag{6.2}$$

Together, the co-spectrum and quadrature spectrum can be used to determine the phase angle, ϕ, between v and ρ (Lumley & Panofsky 1964):

$$\tan(\phi) = \frac{Qu_{v\rho}}{Co_{v\rho}}. \tag{6.3}$$

When $\phi = 0$, v and ρ are in phase and the turbulence is actively stirring the fluid (down-gradient mixing). Counter-gradient fluxes are present when $\phi = \pm\pi$. In this case, negative (positive) vertical velocity fluctuations are coincident with positive (negative) density fluctuations. Internal wave motions are characterized by $\phi = \pm\pi/2$ (Holt *et al.* 1992).

The phase angle data further demonstrate the significance of the vertical Froude number. In figure 20(*a*) the phase angle, ϕ, is shown for the $Ri_b = 0.24$ and $Ri_b = 1.18$ simulations in the source region ($y^* = 0$). In both cases most scales have $\phi \approx 0$, indicating that the source creates turbulence which mixes the fluid. The turbulent Froude number at this location is much larger than unity (owing to a weak density gradient and intense kinetic energy). Near the source there are no counter-gradient fluxes, regardless of Ri_b.

The phase angles for $Ri_b = 0.24$ and $Ri_b = 1.18$ at the location at which $Fr_v = 1$ are shown in figure 20(*b*). In the strongly stratified case the turbulent Froude number reaches unity at $y^* = 1.45$ while in the $Ri_b = .24$ simulation this occurs at $y^* = 1.7$. When $Fr_v = 1$ the turbulence is controlled by stratification and only a few large eddies penetrate far into the quiescent fluid. In both cases the largest scales continue to actively mix. However, the mid-range scales have phase angles of $\pm\pi$, consistent with the counter-gradient fluxes that were described in the contour plot (figure 9). Owing to stable stratification, large scales that penetrate the interface expend much of their kinetic energy raising heavy fluid into the mixed layer. If a parcel of heavy fluid is not mixed by smaller scales it will eventually sink, creating counter-gradient buoyancy flux. However, relative to down-gradient mixing, the counter-gradient fluxes are weak (counter-gradient fluxes are too small to be visible in figure 8). A few of the high wavenumbers indicate internal wave motions ($\phi = \pm\pi/2$), but most of the smallest scales generally yield down-gradient fluxes ($\phi \approx 0$). The kinetic energy at high wavenumbers is derived from restratification occurring at the medium scales and not by a cascade of energy from the large scales.

The minimum of Fr_v for the $Ri_b = 0.24$ and $Ri_b = 1.18$ flows occurs at $y^* = 2$ and $y^* = 1.75$, respectively. The phase angles at these locations are shown in figure 20(*c*). The counter-gradient fluxes have weakened significantly; this is consistent with figure 9. The large scales have highly scattered values of ϕ, many of which are near $\pm\pi/2$. Weak mixing continues at the highest wavenumbers. The phase angle plots demonstrate the importance of the Froude number in characterizing the local state of the turbulence: data for a wide range of Ri_b collapse well with Fr_v.

In figure 21, the buoyancy flux ($g\overline{v\rho}/\rho_o$) is plotted against the vertical Froude number. In the interface region, where Fr_v is a minimum, the buoyancy flux rapidly decreases. Although internal waves and counter-gradient fluxes are active at this Froude number, the rapidly decreasing kinetic energy is responsible for much of the observed decrease in $g\overline{v\rho}/\rho_o$. To isolate the decrease in buoyancy flux caused by

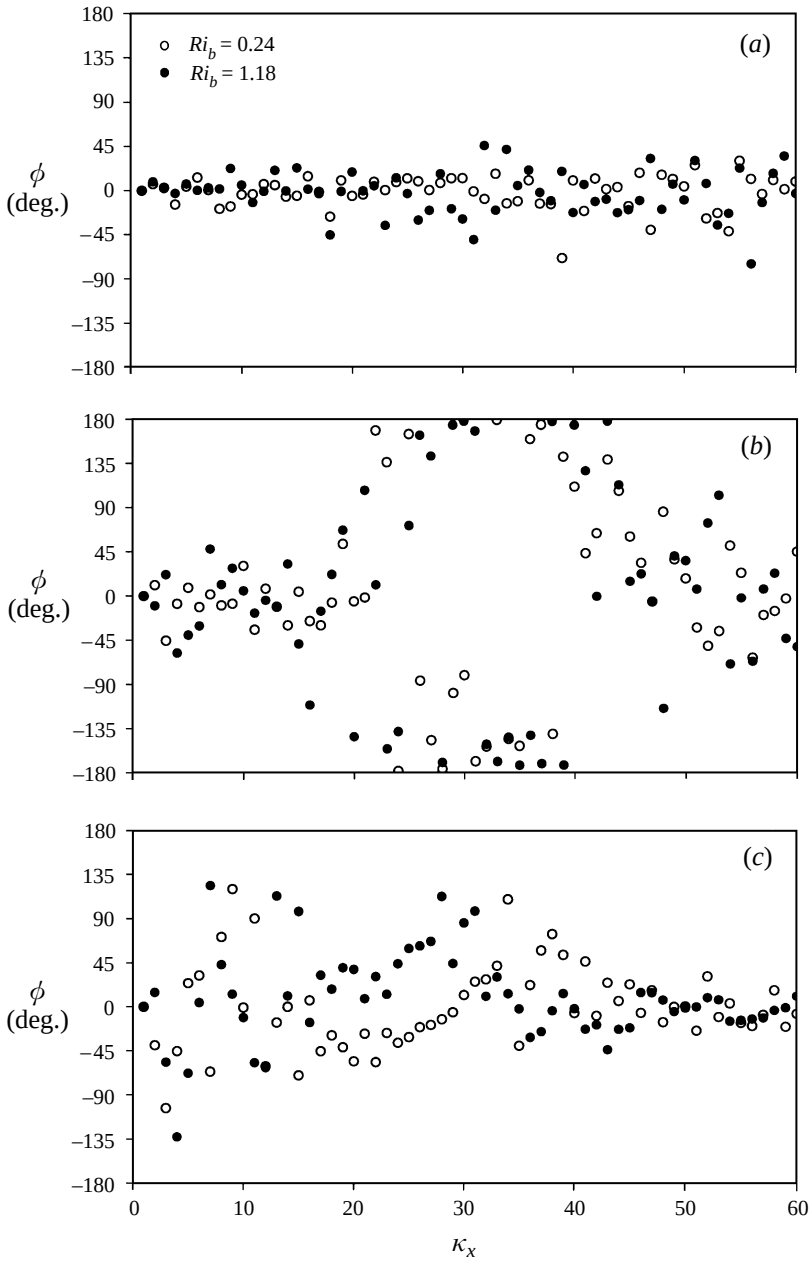

FIGURE 20. Phase angles of the buoyancy flux for $Ri_b = 0.24$ and $Ri_b = 1.18$ at $t^* = 10.6$: (*a*) centre of the source region ($Fr_v > 1$); (*b*) $Fr_v = 1.0$; (*c*) $Fr_v = 0.7$ (minimum Fr_v).

internal waves and counter-gradient flux, the normalized buoyancy flux correlation, $R_{v\rho}$, is analysed. This correlation is plotted against Fr_v in figure 22 along with data from other stratified flows. For $Fr \gg 1$ (near the source), $R_{v\rho}$ is approximately 0.6, which agrees well with the results of homogeneous simulations (Holt *et al.* 1992) and the experimental data of Ivey & Imberger (1991) for $Pr \approx 1$. As the interface is approached ($Fr_v \rightarrow 1$) internal waves and counter-gradient fluxes rapidly reduce $R_{v\rho}$.

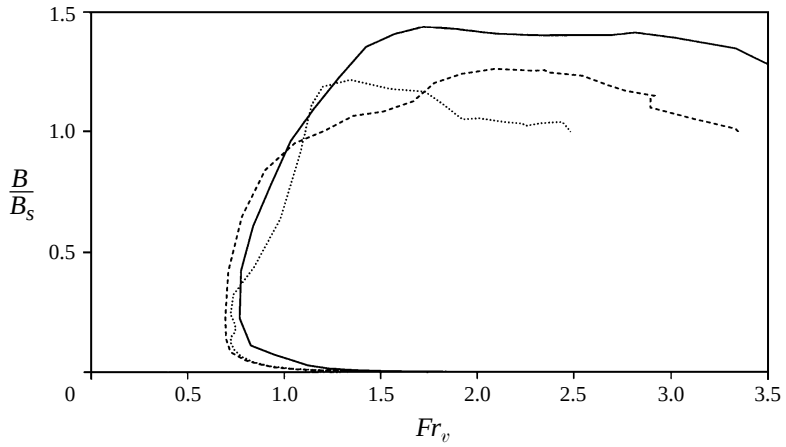

FIGURE 21. Profile of the buoyancy flux at $t^* = 10.6$, normalized by the value at $y^* = 0$ as a function of Fr_v: ——, $Ri_b = 0.24$; – – – –, $Ri_b = 0.47$; · · · ·, $Ri_b = 1.18$.

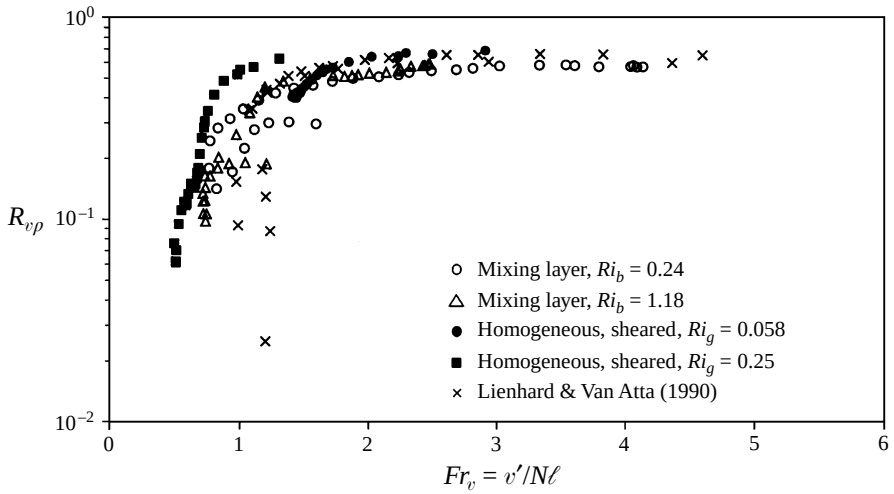

FIGURE 22. Development of the vertical velocity–density correlation coefficient with Fr_v.

In this region the time scale of the large scales (L_E/v) is close to the buoyancy time scale (N^{-1}) and the probability of turbulence generating internal waves is greatly increased owing to resonance. All flows also exhibit similar Fr_v dependence.

6.1. *Energy in the internal wave field*

A more quantitative analysis of the internal wave energy is now presented. Linear internal waves are solutions to the Taylor–Goldstein equation

$$c^2(D^2 - \alpha^2)\Phi + N^2\Phi = 0, \tag{6.4}$$

where $\alpha = (\kappa_x^2 + \kappa_z^2)^{1/2}$ is the horizontal wavenumber (Drazin & Reid 1981). Equation (6.4) is a regular self-adjoint Sturm–Liouville problem with eigenvalues $1/c^2$; the eigenfunctions Φ depend on the profile $N(y)$. A general eigenvalue solver is used to compute the solutions of (6.4) using zero-gradient boundary conditions.

The Fourier coefficients of the velocity field are then projected onto the basis

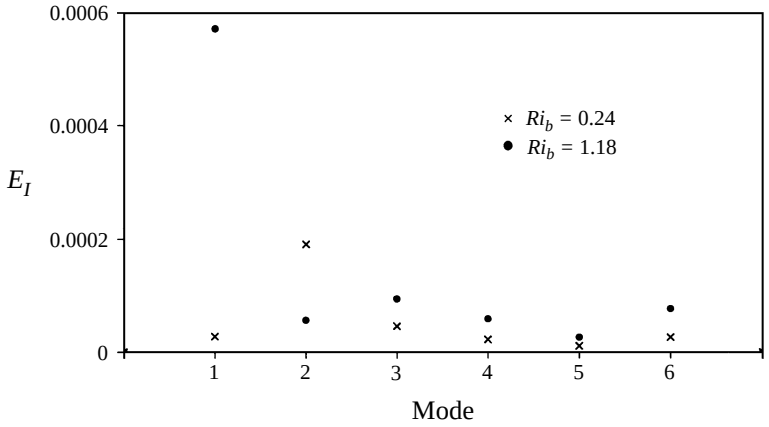

FIGURE 23. Energy in the six most energetic modes of the Taylor–Goldstein equation.

functions

$$\hat{u}(\alpha, y) = \sum_i a_i \Phi_i(\alpha, y), \tag{6.5}$$

where a_i is a weighting coefficient (repeated indices do not imply summation in this section). Application of orthogonality allows the explicit computation of a_m:

$$a_m = \frac{\int_0^{2\pi} N^2 \Phi_m \hat{u}(\alpha, y)\, \mathrm{d}y}{\int_0^{2\pi} N^2 \Phi_m \Phi_m \,\mathrm{d}y}. \tag{6.6}$$

The internal wave energy in the ith mode is found by summing over horizontal wavenumbers

$$E_{I\,i} = \sum_\alpha a_i(\alpha) a_i^*(\alpha). \tag{6.7}$$

The energy can then be computed for each flow using the velocity field and $N(y)$ in well-developed fields ($t^* > 10$). Figure 23 shows the energy in the six most energetic modes. With the exception of the second mode, the energy in the internal wave field generally increases with stratification. The more stratified (higher Ri_b) flows evolve to lower values of Fr_v, enabling internal waves to be more active. It is difficult to quantify the amount of turbulence kinetic energy that is transformed into wave energy. However, observation of the strongly stratified interface reveals that flattening and scouring are the dominant mechanisms and internal wave breaking is not apparent. Interface fluid is transported into the mixed layer by being wrapped around a rotating large eddy.

7. Conclusions

Direct numerical simulations were used to investigate the turbulence structure and physical mechanisms of mixing at a shear-free stratified interface. The turbulence source, located above the interface, is fixed and the bulk Richardson number is varied. The collapse of the data with local Froude number, consistent with results from homogeneous stratified flows, underscores the importance of local parameters in the analysis of stratified turbulence.

Kinetic energy budgets in the interface region quantify the importance of turbulence transport. Under unstratified conditions, turbulence transport balances dissipation and pressure transport. In weakly stratified flow, all of the terms in the budget are reduced near the interface. Turbulence transport rapidly decreases as the large eddies flatten at the interface. Energy transported into the interface region is converted into buoyancy flux and dissipation. In highly stratified (buoyancy dominated) flow, turbulence transport is extinguished at the interface. Pressure transport becomes positive, balancing dissipation and buoyancy flux, and internal waves become active.

Turbulence structure can be characterized by local Froude number for fixed Re and Pr. Large engulfing structures that appear under weakly stratified conditions ($Fr_v > 1$) cause the interface to become highly distorted and contribute to mixing. When stratification intensifies, the interface acts as a barrier to turbulence diffusion and large-scale overturns become impossible. Eddies moving downward from the source stall at the interface. If the eddies have large horizontal vorticity, scouring can occur.

Turbulence transport spectra show that the large scales are responsible for most of the energy transport into the interface region. As stratification increases, energy at low wavenumbers is reduced. Without large-scale overturns, spectral transfer of energy from the large to small scales is also decreased. The buoyancy flux is predominately down-gradient and occurs at the large scales. However, weak counter-gradient fluxes at the medium to small scales are observed far from the source as parcels of fluid stirred by the large scales restratify.

Internal waves are generated by the turbulence in the interface region where the Froude number is minimum. The phase angle between velocity and density in the large scales is close to $\pm\pi/2$ here and the correlation between density and vertical velocity rapidly decreases. The energy in the linear internal wave modes, determined by projecting onto Taylor–Goldstein solutions, generally increases with stratification at low wavenumber.

The vertical turbulent Froude number characterizes many features of stratified turbulence including mixing efficiency, turbulence structure, and counter-gradient fluxes. Use of the anisotropy of the turbulence also improves the correlation of turbulence mixing with stable stratification. Incorporating anisotropy information into the definition of the mixing efficiency allows data from various stratified turbulent flows to collapse when plotted with Fr_v. The vertical mixing efficiency (η_v) is larger than the isotropic mixing efficiency defined by Ivey & Imberger (1991) because it emphasizes the anisotropy in the flow. Turbulent flows with more energy in the horizontal component do not mix as effectively as flows with most of the energy in the vertical component.

The Reynolds numbers in the simulations presented in this paper are fairly low: $Re_\lambda = 60$ in the source region. As a result, the turbulence may be influenced by viscous effects. However, earlier work (Holt *et al.* 1992, among others) shows that effects of Reynolds number essentially disappear when this parameter large enough. The definition of 'large enough' may be flow dependent but a reasonable criterion seems to be $Re_\lambda \geqslant 25$. All of the flows in this paper are in this regime. Further support for the argument that viscous effects are not important is provided by the generally excellent agreement with the experimental data, all of which were taken at somewhat higher Reynolds numbers.

The authors also wish to thank the Office of Naval Research for support of this work through grant number N00014-92-J-1611, monitored by Dr L. Goodman.

REFERENCES

Breidenthal, R. E. 1992 Entrainment at thin stratified interfaces: The effects of Schmidt, Richardson, and Reynolds numbers. *Phys. Fluids* A **4**, 2141–2144.

Briggs, D. A. 1996 Turbulent entrainment in a shear-free stably stratified two-layer fluid. PhD thesis, Stanford University, Stanford, California.

Briggs, D. A., Ferziger, J. H., Koseff, J. R. & Monismith, S. G. 1996 Entrainment in a shear-free turbulent mixing layer. *J. Fluid Mech.* **310**, 215–241.

Denton, R. A. & Wood, I. R. 1981 Penetrative convection at low Peclet number. *J. Fluid Mech.* **113**, 1–21.

De Silva, I. P. D. & Fernando, H. J. S. 1992 Some aspects of mixing in a stratified turbulent patch. *J. Fluid Mech.* **240**, 601–625.

Drazin, P. G. & Reid, W. H. 1981 *Hydrodynamic Stability*. Cambridge University Press.

E, X. & Hopfinger, E. J. 1986 On mixing across an interface in stably stratified fluids. *J. Fluid Mech.* **166**, 227–244.

Ellison, T. H. & Turner, J. S. 1959 Turbulent entrainment in stratified flows. *J. Fluid Mech.* **6**, 423–448.

Fernando, H. J. S. 1991 Turbulent mixing in stratified fluids. *Ann. Rev. Fluid Mech.* **23**, 455–93.

Fernando, H. J. S. & Long, R. R. 1985 On the nature of the entrainment interface of a two-layer fluid subjected to zero-mean-shear turbulence. *J. Fluid Mech.* **151**, 21–53.

Gerz, T., Schumann, U. & Elghobashi, S. E. 1989 Direct numerical simulation of stratified homogeneous turbulent shear flows. *J. Fluid Mech.* **200**, 563–594.

Hannoun, I. A., Fernando, H. J. S. & List, E. J. 1988 Turbulence structure near a sharp density interface. *J. Fluid Mech.* **189**, 189–209.

Holt, S. E., Koseff, J. R. & Ferziger, J. H. 1992 A numerical study of the evolution and structure of homogeneous stably stratified sheared turbulence. *J. Fluid Mech.* **237**, 499–539.

Hopfinger, E. J. & Toly, J.-A. 1976 Spatially decaying turbulence and its relation to mixing across density interfaces. *J. Fluid Mech.* **78**, 155–175.

Imberger, J. & Head, R. 1994 *Measurement of Turbulent Properties in a Natural System. Proc. ASME Symp. on Fundamentals and Advancements in Hydraulic Measurements and Experimentation, Buffalo, NY, USA, Aug. 1–5, 1994.*

Itsweire, E. C. & Helland, K. N. 1989 Spectra and energy transfer in stably stratified turbulence. *J. Fluid Mech.* **207**, 419–452.

Itsweire, E. C., Helland, K. N. & Van Atta, C. W. 1986 The evolution of grid-generated turbulence in a stably stratified fluid. *J. Fluid Mech.* **162**, 299–338.

Itsweire, E. C., Koseff, J. R., Briggs, D. A. & Ferziger, J. H. 1992 Turbulence in stratified shear flows: Implications for interpreting shear-induced mixing in the ocean. *J. Phys. Oceanogr.* **23**, 1508–1522.

Ivey, G. N. & Imberger, J. 1991 On the nature of turbulence in a stratified fluid. Part I: The energetics of mixing. *J. Phys. Oceanogr.* **21**, 650–658.

Ivey, G. N., Koseff, J. R., Briggs, D. A. & Ferziger, J. H. 1992 Mixing in a stratified shear flow: energetics and sampling. *Annual Research Briefs 1992*, pp. 334-341. Center for Turbulence Research, Stanford University.

Kantha, L. H., Phillips, O. M. & Azad, R. S. 1977 On turbulent entrainment at a stable density interface. *J. Fluid Mech.* **79**, 753–768.

Lienhard, J. H. & Van Atta, C. W. 1990 The decay of turbulence in thermally stratified flow. *J. Fluid Mech.* **210**, 57–112.

Linden, P. F. 1973 The interaction of a vortex ring with a sharp density interface: A model for turbulent entrainment. *J. Fluid Mech.* **60**, 467–480.

Linden, P. F. 1975 The deepening of a mixed layer in a linearly stratified fluid. *J. Fluid Mech.* **71**, 385–405.

Lumley, J. L. & Panosfky, H. A. 1964 *The Structure of Atmospheric Turbulence*. New York: Interscience.

Nokes, R. I. 1988 On the entrainment rate across a density interface. *J. Fluid Mech.* **188**, 185–204.

Ozmidov, R. V. 1965 On the turbulent exchange in a stably stratified ocean. *Atmos. Ocean Phys.* **10**, 83.

Piccirillo, P. 1993 An experimental study of the evolution of turbulence in a uniformly sheared thermally stratified flow. PhD thesis, University of California, San Diego.

Rogallo, R. S. 1981 Numerical experiments in homogeneous turbulence. *NASA Tech. Memo*. 81315.

Rohr, J. J., Itsweire, E. C., Helland, K. N. & Van Atta, C. W. 1988 Growth and decay of turbulence in a stably stratified shear flow. *J. Fluid Mech.* **195**, 77–111.

Sullivan, G. D. & List, E. J. 1994 On mixing and transport at a sheared density interface. *J. Fluid Mech.* **273**, 213–239.

Thompson, S. M. & Turner, J. S. 1975 Mixing at an interface due to turbulence generated by an oscillating grid. *J. Fluid Mech.* **67**, 349–368.

Turner, J. S. 1968 The influence of molecular diffusivity on turbulent entrainment across a density interface. *J. Fluid Mech.* **33**, 639–656.

Winters, K. B., Lombard, P. N., Riley, J. J. & D'Asaro, E. A. 1995 Available potential energy and mixing in density-stratified fluids. *J. Fluid Mech.* **289**, 115–128.

Zauderer, E. 1989 *Partial Differential Equations of Applied Mathematics*. Wiley Interscience.